Interconversion of sp-hybridized chemical bonds induces piezoelectric enhanced photocatalysis

Wenbo Feng [b], Yujie Jiang [a], Fuguo Ge [a,c], Qiang Bai [a,*], Jun Yang [d], Limin Shang [a], Rui Cao [a], Gang Niu [d,e], Lina Wang [b,*], Zhiling Zhu [a,*], Ning Sui [a,*]

[a] College of Materials Science and Engineering, Qingdao University of Science and Technology, 53 Zhengzhou Road, Qingdao, Shandong 266042, China
[b] College of Environment and Safety Engineering, Qingdao University of Science and Technology, 53 Zhengzhou Road, Qingdao, Shandong 266042, China
[c] College of Information Science and Technology, Qingdao University of Science and Technology, Qingdao, Shandong 266042, China
[d] State Key Laboratory for Manufacturing Systems Engineering; Electronic Materials Research Laboratory, Key Laboratory of the Ministry of Education, School of Electronic Science and Engineering, Xi'an Jiaotong University, Xi'an, Shanxi 710049, China
[e] The International Joint Laboratory for Micro/Nano Manufacturing and Measurement Technology, Xi'an Jiaotong University, Xi'an, Shanxi 710049, China

ABSTRACT

The synergism of piezoelectric catalysis and plasmonic photocatalysis is an effective approach for enhancing the catalytic performance. Nevertheless, challenges remain in addressing the slow interfacial charge transfer rate and the high recombination of energetic hot electrons. In this study, we constructed a heterostructure comprising barium titanate/graphdiyne/gold nanofibers (BTO/GDY/Au NFs). The incorporation of a graphdiyne (GDY) layer serves as an electron sponge, significantly boosting the piezo-photocatalytic activity, with a degradation rate constant 3.3-fold higher than that of BTO/Au. Theoretical calculations indicated that BTO could undergo elastic deformation under ultrasound irradiation, resulting in the stretching and compression of GDY within a lattice constant range of 7.1–10.4 Å. This deformation induced the reversible conversion of sp-hybridized C≡C to C=C, releasing electrons that could recombine with hot holes generated by the Au nanoparticles (Au NPs). Consequently, more hot electrons were able to participate in the catalytic reaction process. Furthermore, BTO/GDY/Au NFs demonstrated excellent catalytic performance in the rapid degradation of organic dyes and antibiotics in wastewater, while also inhibiting bacterial propagation. The above-mentioned results validated the feasibility of this heterostructure for practical applications. Overall, this study presents a novel piezo-photocatalysts, where the interconversion of sp-hybridized chemical bonds in GDY can serve as electron donor, thus significantly enhancing piezo-photocatalysis.

1. Introduction

Piezo-photocatalysis represents an advanced green technology that harnesses the synergistic effect of photocatalysis and non-centrosymmetric semiconductor piezoelectronics, combining mechanical and light energy [1–7]. Metal nanostructures with characteristic localized surface plasmon resonance (LSPR) exhibit tunable absorption properties and generate energetically favorable hot carriers in the visible range [8–12]. By integrating the piezoelectric effect with the LSPR effect, the built-in electric field resulting from the mechanically stimulation-induced polarization can contribute to the separation of hot electrons and holes generated through photoexcitation. This efficient modulation of charge migration behavior at the interface [13], along

with the synergistic effects of LSPR and piezoelectric optoelectronics, can further enhance the photocatalytic activity [14–16]. Current research has explored, the combination of the LSPR effect with piezo-photocatalysis to enhance the catalytic activity and this enhancement involves utilizing the coupling of surface hot electrons and piezoelectric effect within heterostructures [17], e.g., Ag/BaTiO$_3$ [18–20], Pt/BaTiO$_3$ [21], Au/AgNbO$_3$ [22], and Au/MoS$_2$ [23]. However, a limitation arises from the migration of separated electrons and holes in piezoelectric semiconductors towards the surface of the catalyst, where rapid recombination occurs on the surface, hindering efficient space charge separation and severely limiting the transport between the interfaces formed with other active materials [24–26]. Furthermore, the mismatch between the short lifetime of the hot carriers (femtosecond to

nanosecond scale) and the long time scale of the chemical reaction (spanning milliseconds to seconds) due to the LSPR effect further inhibits the catalytic activity and efficiency of plasmonic photocatalysis [27–29]. Accordingly, it is crucial to enhance the catalytic efficiency of photocatalysts by increasing the charge transfer rate and decreasing the recombination rate of hot electron-hole pairs.

The incorporation of an intermediate semiconductor layer between semiconductor material and LSPR nanomaterials, forming a three-phase heterostructure, has emerged as an advanced strategy to tackle down the above mentioned problems [30–32]. The continuous charge migration at the interface of the three-phase heterostructure can be facilitated by introducing a suitable intermediate layer, effectively suppressing the recombination of hot electrons and holes, which in turn promotes the involvement of a greater number of hot electrons in the catalytic reaction, ultimately enhancing the overall catalytic activity [33–35]. Zhou et al. illustrated the use of a multiphase heterostructure, where PbS was inserted between Au NPs and WO_{3-x} in a photocatalytic system. This insertion can improve the charge separation and result in a 2.4-fold increase in photocatalytic activity, primarily attributed to the narrow band gap of PbS [32]. Consequently, the insertion of a layer of narrow bandgap semiconductor material with matched energy level structure holds promise for mitigating charge recombination phenomena and facilitating the participation of more electrons and holes in catalytic reactions [36]. GDY refers to a narrow bandgap semiconductor [37], which is considered an emerging and distinctive carbon allotrope comprising of an aromatic ring and a carbon-carbon triple bond (sp-hybridized carbon) with a high degree of π-π conjugation tunable electronic properties, and prominent electron-transferring and electron-storing abilities [38–41]. The above-mentioned structural and property characteristics highlight the potential of GDY as an intermediate for the improvement of piezo-photocatalysis [42–44]. Au NPs are universal and typical in plasmon catalyzed reactions due to their stability and tunable visible light absorption [45]. Barium titanate (BTO) with high dielectric constants exhibits excellent piezoelectric effect under mechanical energy stimulation [46–49]. In this study, we aimed to insert a layer of GDY between BTO and Au NPs. GDY with a narrow bandgap and energy levels matching those of BTO can facilitate the efficient separation of electrons and holes by forming a heterostructure of BTO/GDY/Au NFs [50,51]. Furthermore, previous reports have indicated that under the influence of an ultrasound field, carbon-carbon triple bonds (C≡C) in GDY can be converted to double bonds (C═C), releasing electrons [52–54]. These electrons are expected to combine with hot holes of Au NPs, further augmenting the participation of hot electrons in the catalytic reaction and consequently improving the piezo-photocatalytic activity.

This study focused on the design of three-phase heterostructure, specifically BTO/GDY/Au NFs, for piezoelectric-enhanced photocatalysis. The incorporation of BTO with its excellent piezoelectric properties, along with the reversible conversion of sp-hybridized C≡C to C═C in GDY under ultrasound stimulation, plays a crucial role in this system. The released electrons from GDY were then recombined with hot holes on the surface of Au NPs, effectively inhibiting the recombination of hot electron-hole pairs and thereby promoting photocatalytic activity. The experimental results demonstrated that the degradation rate constant of BTO/GDY/Au NFs was 3.3-fold higher compared with that of BTO/Au under the combined influence of light and ultrasound. Moreover, BTO/GDY/Au NFs possessed remarkable efficiency in degrading wastewater pollutants, achieving a degradation efficiency of 97.2% for methylene blue (MB) within 30 min timeframe. Furthermore, the bactericidal effect of BTO/GDY/Au NFs against methicillin resistant *Staphylococcus aureus* (MRSA) and *Escherichia coli* (*E. coli*) is noteworthy, with a bactericidal efficiency of 99.999%.

2. Experimental section

2.1. Materials

All chemicals utilized in this study are described in the Supporting Information.

2.2. Synthesis of BTO/GDY/Au NFs

The synthesis of BTO NFs and BTO/GDY NFs. The procedure for synthesizing BTO NFs has been previously reported [55]. GDY was primarily synthesized on diatomite through Glaser-Hay coupling reaction using hexaethynylbenzene (HEB) as the monomer. To initiate the reaction, a solution of HEB-TMS and tetra-n-butylammonium fluoride (TBAF, 1 M in THF) was prepared under an argon atmosphere and stirred at 0 °C for 15 min. Subsequently, the mixture was diluted with ethyl acetate, subjected to two washes with saturated sodium chloride (NaCl) solution, dried using anhydrous magnesium sulfate ($MgSO_4$), and filtered. The solvent was evaporated under vacuum while maintaining the temperature below 20 °C. The resulting residue was diluted in 50 mL of acetone and added dropwise over a period of 10 h into a three-necked flask containing acetone (100 mL), pyridine (5 mL), BTO (20 mg). The reaction mixture was maintained at 60 °C for 15 h under an argon atmosphere. It is important to note that all processes, from deprotection to addition, should be carried out in darkness at low temperature to prevent the decomposition of HEB. Upon completion of the reaction, the GDY flakes were grown on the BTO and subsequently washed sequentially with N,N-dimethylformamide (DMF), acetone, and ethanol. Finally, the BTO/GDY composite was subjected to freeze-drying.

The synthesis of BTO/GDY/Au NFs. 10 mg BTO/GDY NFs, 52 μL $HAuCl_4·3 H_2O$ (48.56 mM) and 1 mg sodium citrate were combined and stirred. Subsequently, 1 mL $NaBH_4$ (1 mg mL^{-1}) was added to the mixture. After 10 min, the resulting material was washed with deionized water three times and then subjected to freeze-drying.

2.3. Electrochemical characterizations

The photoelectrochemistry was performed using an electrochemistry workstation (PGSTAT302N, Metrohm Autolab B.V., The Netherlands). A standard three electrode system was employed, comprising a Pt counter electrode, an Ag/AgCl reference electrode, and a GCE as the working electrode. The GCE working electrode was prepared by drop-coating a solution of BTO, BTO/Au, and BTO/GDY/Au NFs solution onto a clean electrode (0.07 cm^2). Next, the coated electrode was dried in a vacuum oven for 3 h. Electrochemical impedance spectroscopy (EIS) was conducted in a Na_2SO_4 electrolyte (0.1 M) with an open circuit voltage and a frequency range of 0.01–10^5 Hz. The Xenon lamp and ultrasound was used to excite the current in a Na_2SO_4 electrolyte (0.5 M) at 0.4 V bias potential.

2.4. Performance computation of BTO/GDY/Au NFs under ultrasound

The BTO, GDY and Au materials were modeled and optimized by using CASTEP module of Materials Studio. Perdew-Burke-Ernzerhof (PBE) of Generalized Gradient Approximation (GGA) was selected for calculations, and it was assigned as group A. Subsequently, Au was incorporated into group A to form a simple surface model of GDY covered BTO with loaded gold particles and set it as group B. The electron density difference was computed for both group A and group B by utilizing the Electron density difference of CASTEP module, and the local density of states (DOS) of BTO, GDY, Au, and BTO/GDY was determined by using the Band structure of CASTEP module. Furthermore, the system energies corresponding to the protocells of BTO and GDY with different lattice constants were calculated individually by using the PBE of GGA in the CASTEP module.

2.5. Degradation of dyes and antibiotics

The catalytic performance of BTO/GDY/Au NFs was evaluated by using a discoloration model of MB. In this study, the BTO/GDY/Au NFs (100 mg L^{-1}) were dispersed in a MB solution (10 mg L^{-1}, pH=4) in a glass beaker. The mixture was stirred at ambient temperature in the dark for 30 min. Subsequently, H$_2$O$_2$ (100 mM) was introduced and the mixture solution was then subjected to both light and ultrasound treatment for 30 min. To maintain a consistent temperature during the ultrasound treatment and prevent excessive heating over a long period, ice bags were placed in the ultrasound cleaner, ensuring keep the temperature around 25 °C with the fluctuation less than 0.5 °C. The MB discoloration was monitored by using a UV–vis spectrophotometer. During the reaction, 1 mL of samples were withdrawn at specific time intervals and centrifuged to collect the supernatant for subsequent analysis. The removal efficiency was calculated by determining the relative concentration (C/C$_0$) as a function of time by the following equations:

$$\text{Removal Efficiency}(\%) = \frac{C}{C_0} \times 100\% = \frac{A}{A_0} \times 100\% \quad (1)$$

$$-\ln\text{RE} = kt \quad (2)$$

where A$_0$ denotes the absorbance of the initial MB solution, C$_0$ represents the initial concentration of MB, A is the absorbance of the MB solution after a given time of the reaction, C expresses the residual concentration of MB after a given time of the reaction. k is the reaction rate constant of MB degradation; t denotes the reaction time. The absorbance was measured at 663 nm.

The degradation cycle experiment was performed by repeatedly adding MB (10 mg mL^{-1}) into the mother solution. Furthermore, miscellaneous dyes (Rhodamine B (Rh B), Methyl Orange (MO), Congo Red) at 10 mg L^{-1} and antibiotics (tetracycline, penicillin, ciprofloxacin, and rifampin) at 20 mg L^{-1} were prepared respectively. These compounds were used for a broad-spectrum degradation test following to the above-mentioned method.

2.6. Analysis of the MB degradation intermediates by electrospray ionization mass spectrometry (ESI-MS)

MB degradation products were analyzed through ESI-MS in the positive ion mode [56]. An optimization procedure at the beginning of this work was conducted to ensure optimal signal intensity. The ESI spray conditions were set as follows: capillary voltage at 4500 V, drying gas temperature at 180 °C, dry gas flow rate of 4 L min^{-1}, end plate offset of 500 V, as well as nebulizer pressure at 0.3 bar. All MS measurements were performed with an accumulated ESI-MS time of 5 min. The peak patterns were within the *m/z* range of 100–350.

2.7. Bacterial cell culture

The bacterial strains employed this study were MRSA and *E. coli*. These strains were obtained from China General Microbiological Culture Collection Center (CGMCC). Prior to the experiments, the bacteria were typically cultured in LB medium in an orbital shaker at 200 rpm for overnight incubation at 37 °C. Subsequently, a small quantity of the overnight culture was transferred to an LB agar plate. For each experiment, a single colony of MRSA or *E. coli* was selected from the LB agar plate and cultured in LB media for 12 h at 37 °C and 200 rpm. Following the incubation period, the bacterial culture was centrifuged at 4000 rpm for 5 min to pellet the cells. The resulting pelleted cells were then washed three times with PBS to eliminate any remaining macromolecules and other components of the growth media. The quantity of bacterial suspension was determined by measuring the optical density at 600 nm (OD$_{600}$) using a UV–visible spectrophotometer (UV-2900,

Hitachi Co, Japan).

2.8. Elimination of microorganisms in wastewaters

Microbiologically polluted wastewater (1 × 10^7 CFU mL^{-1}) was prepared by mixing fresh bacterial suspensions with domestic sewage, seawater, river water, and industrial wastewater, respectively. Subsequently, BTO/GDY/Au NFs (200 mg L^{-1}) and H$_2$O$_2$ (200 mM) were added to microbial and dye-contaminated wastewater (10 mL), under light and ultrasound for 30 min. After completion, serial dilutions of the mixture solution (1, 10^{-2}, 10^{-4}, 10^{-6}) were prepared and a 100 μL of aliquot was plated on the LB agar. The bacterial colonies formed after 24 h static incubation at 37 °C were counted. The microorganism contaminated wastewater without any treatment was served as control groups.

2.9. Morphological observation of BTO/GDY/Au NFs treated bacteria

The morphology of bacteria treated with BTO/GDY/Au NFs was examined by employing a Scanning Electron Microscope (SEM) [57]. In a sterile culture tube, BTO/GDY/Au NFs (0.1 mg mL^{-1}) and H$_2$O$_2$ (16 mM) were combined with a new bacterial suspension (1×10^7 CFU mL^{-1}) in PBS at pH=7.4. The mixture solution was then subjected to light and ultrasound treatment for 5 min. The bacteria that had been exposed to BTO/GDY/Au NFs were then collected through centrifugation at 5000 rpm and thoroughly cleaned with PBS three times. The pellets were gathered and fixed in a 2.5% glutaraldehyde solution for 6 h at 4 °C, followed by 0.1% OsO$_4$ solution at 4 °C for 6 h. Next, the fixed bacteria were dehydrated with a gradient of 25, 50, 75, 90, and 100% ethanol for a total of 15 min, followed by 100% t-butanol. After being lyophilized and sputter-coated, the samples were analyzed using a SEM at an 8 kV accelerating voltage. For the control group, bacteria treated with BTO/GDY/Au NFs and H$_2$O$_2$ but not subjected to light and ultrasound treatment were employed.
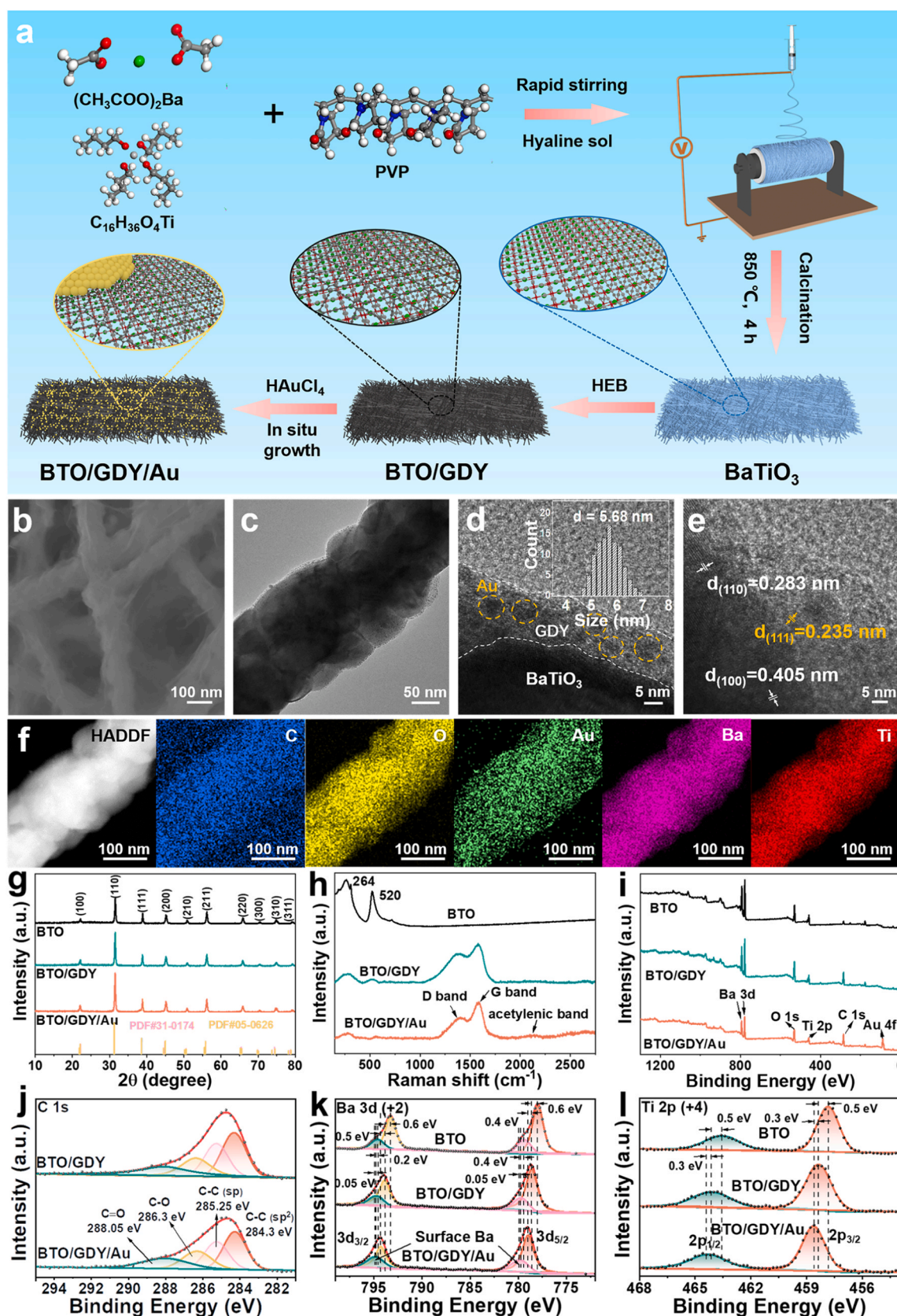
2.10. Statistical analysis

The data was presented as mean ± standard deviation (S.D.). Statistical analyses were performed in triplicate unless otherwise noted. Statistical comparisons were made using Student's t-test and one-way one-way analysis of variance (ANOVA). Tukey's multiple comparison test was used after ANOVA to assess statistical differences in the 2016 Microsoft Excel version (Microsoft Corporation, USA). * p < 0.05, ** p < 0.01, and *** p < 0.001.

3. Results and discussion

3.1. Preparation and characterization of BTO/GDY/Au NFs

Fig. 1a illustrates the synthesis method of BTO/GDY/Au NFs. BTO was synthesized through electrostatic spinning with barium acetate and tetrabutyl titanate, followed by the in situ growth of GDY nanosheets around the prepared BTO. Lastly, Au NPs were deposited on the surface of BTO/GDY to obtain the BTO/GDY/Au NFs heterostructure. Fig. 1b displays the SEM images of BTO/GDY/Au NFs, clearly showing GDY nanosheets assembled on the BTO surface (Fig. S1). Fig. 1c, d demonstrates the uniform coating of GDY on the BTO surface and Au NPs were uniformly distributed on the BTO/GDY surface, where the size of Au NPs was 5.68 ± 0.5 nm. The high-resolution transmission electron microscopy images (Fig. 1e) indicate that both BTO and Au NPs crystallize were well crystallized with the preferential crystalline orientations to form heterogeneous structures. The measured lattice spacings of 0.235 nm belonged to the (111) face of the Au NPs, 0.283 and 0.405 nm were well attributed to the (110) and (100) faces of the BTO, respectively. The elemental mapping (Fig. 1f) illustrates that C, O, Au, Ba and Ti were uniformly distributed on the surface of BTO/GDY/Au NFs,

Fig. 1. Synthesis and characterization of BTO/GDY/Au NFs. (a) Synthetic route, (b) SEM, (c, d) TEM and size distribution of Au NPs (inset), and (e) HRTEM image of BTO/GDY/Au NFs. (f) TEM image and EDS elemental maps of BTO/GDY/Au NFs. (g) XRD patterns of BTO, BTO/GDY, and BTO/GDY/Au NFs. (h) Raman spectra of BTO, BTO/GDY, and BTO/GDY/Au NFs. (i) XPS spectra of BTO, BTO/GDY, and BTO/GDY/Au NFs, (j) C 1 s, (k) Ba 3d, and (l) Ti 2p.

indicating that the GDY grew uniformly on the surface of the BTO and the Au NPs were uniformly loaded onto the GDY. The above characterization revealed that the heterostructure of BTO/GDY/Au NFs were successfully prepared.

The crystal structures of the BTO, BTO/GDY and BTO/GDY/Au NFs samples were further observed through X-ray diffraction (XRD). As depicted in Fig. 1g, BTO and BTO/GDY displayed tetragonal crystal structures (PDF#05–0626), with an additional diffraction peak at 38.2° after loading Au NPs belonging to the (111) plane of the face-centered cubic unit cell structure of Au (PDF#65–2870) (Fig. S2), indicating the formation of heterogeneous structures of BTO/GDY/Au NFs [58]. Raman spectrum of BTO/GDY/Au NFs (Fig. 1h) comprised four main peaks, of which, the peaks at 1912 and 2103 cm^{-1} belonged the vibration of diyne links (C≡C-C≡C) and some vibrations were associated with C≡C [59]. Comparison of Raman spectra suggested that the BTO/GDY/Au NFs retained the characteristic peaks of GDY, while the characteristic peaks of BTO were retained at 276 and 527 cm^{-1}. The chemical states of the BTO/GDY/Au NFs were examined through X-ray photoelectron spectroscopy (XPS) (Fig. 1i and Tab. S1). The C1s peak (Fig. 1j) can be reflected as subpeaks of C-C (sp^2), C-C (sp), C-O and C=O with binding energies of 284.3, 285.3, 286.3 and 288.1 eV, respectively. Fig. 1k presents the high-resolution XPS spectra of Ba 3d profiles. In the Ba 3d spectra of the pristine BTO, the peaks of Ba 3d 5/2 and Ba 3d 3/2 were located at 778.0 and 793.3 eV, respectively, corresponding to the Ba atoms in the ABO_3 perovskite structure [60]. The peaks of Ba 3d 5/2 and Ba 3d 3/2 were located at 779.5 and 794.6 eV, respectively, corresponding to the Ba atoms in the non-perovskite structure [61]. In both BTO/GDY and BTO/GDY/Au NFs, the positions of the peaks were shifted toward higher values compared with the original BTO, probably arising from surface defects and lattice distortions in the BTO/GDY and BTO/GDY/Au NFs heterostructure. In the BTO/GDY/Au NFs, the two peaks of Ti 2p at 458.7 and 464.3 eV corresponded to the 2p 3/2 and 2p 1/2 peaks of Ti^{4+}, respectively (Fig. 1l). The high-resolution Au 4 f spectra are depicted in Fig. S3, where 83.6 and 88.0 eV were the signals of the metals Au 4 f 7/2 and 4 f 5/2, and 84.7 and 90.8 eV were the signals of Au^{3+}. The blue-shifted electric couples were surface oxidation products due to the storage of Au^{3+} in the air. Notably, both the binding energy positions of the Ba 3d and Ti 2p peaks of BTO/GDY are shifted left when compared to BTO, indicating a transfer of electrons from BTO to GDY. BTO, BTO/GDY, and BTO/GDY/Au NFs exhibit almost superimposable Fourier transform infrared (FTIR) spectra (Fig. S4), and the peak at 578 cm^{-1} corresponds to the stretching vibration of Ti-O in the BTO crystal. The strong peaks around 3444 and 1632 cm^{-1} corresponded to stretching vibration and inplane bending vibration peaks of -OH groups, as derived from water molecules adsorbed on the surface.

3.2. Optical and piezoelectric properties of BTO/GDY/Au NFs

The piezoelectric properties of the BTO/GDY/Au NFs were investigated using piezoelectric force microscopy (PFM). As shown in Fig. S5, the BTO/GDY/Au NFs have a nanofiber morphology with a diameter of about 200 nm. The different positions of The PFM phase and amplitude maps as depicted in Fig. 2a, b, exhibited distinct positions and apparent contrasts in the dark brown and bright yellow regions, respectively. These variations were found to correlate with upward and downward polarization directions, indicating the presence of different polarization orientations. Furthermore, a voltage reversal of 10 V led to a phase reversal close to 180° (Fig. 2c), indicating a high likelihood of dipole alteration in response to an external electric field. Fig. 2c exhibited a clear butterfly-shaped amplitude loop, illustrating the electric field-induced polarization switching behavior and the consequent hysteresis in the strain field. The slight asymmetry observed in the return line of the piezoelectric amplitude hysteresis can be attributed to the inherent internal field and the movement of magnetic domains beneath the tip region. The piezoelectric coefficient (d_{33}) is defined as the ratio of the electric field strength to the stress change when varying stresses are applied to piezoelectric materials. The d_{33} value can be determined by calculating the corresponding slope of the displacement-voltage curve
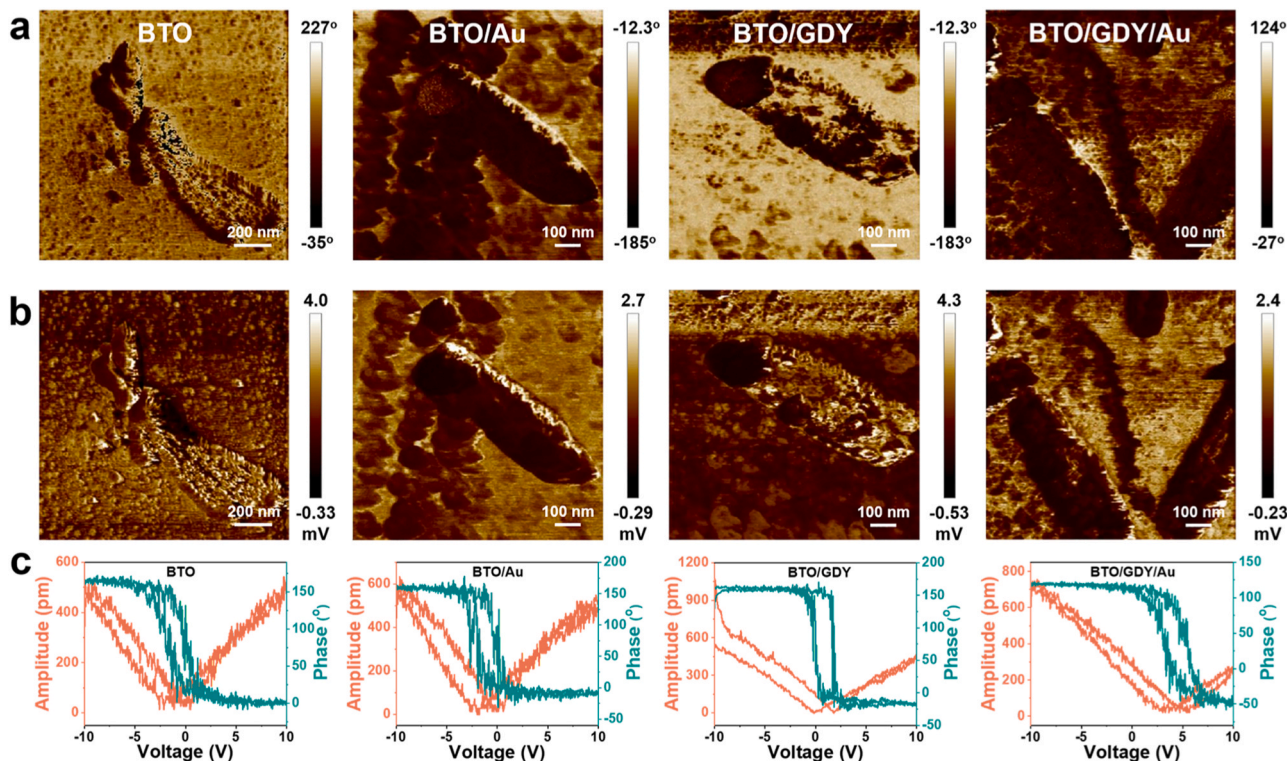

Fig. 2. (a) phase image, (b) amplitude image, and (c) displacement-voltage butterfly loop and phase hysteresis loop of BTO, BTO/Au, BTO/GDY, and BTO/GDY/Au NFs.

using the following equation, where V and A represent the applied voltage and amplitude, respectively; V_0 and A_0 denote the intersection point of the amplitude butterfly loop curve.
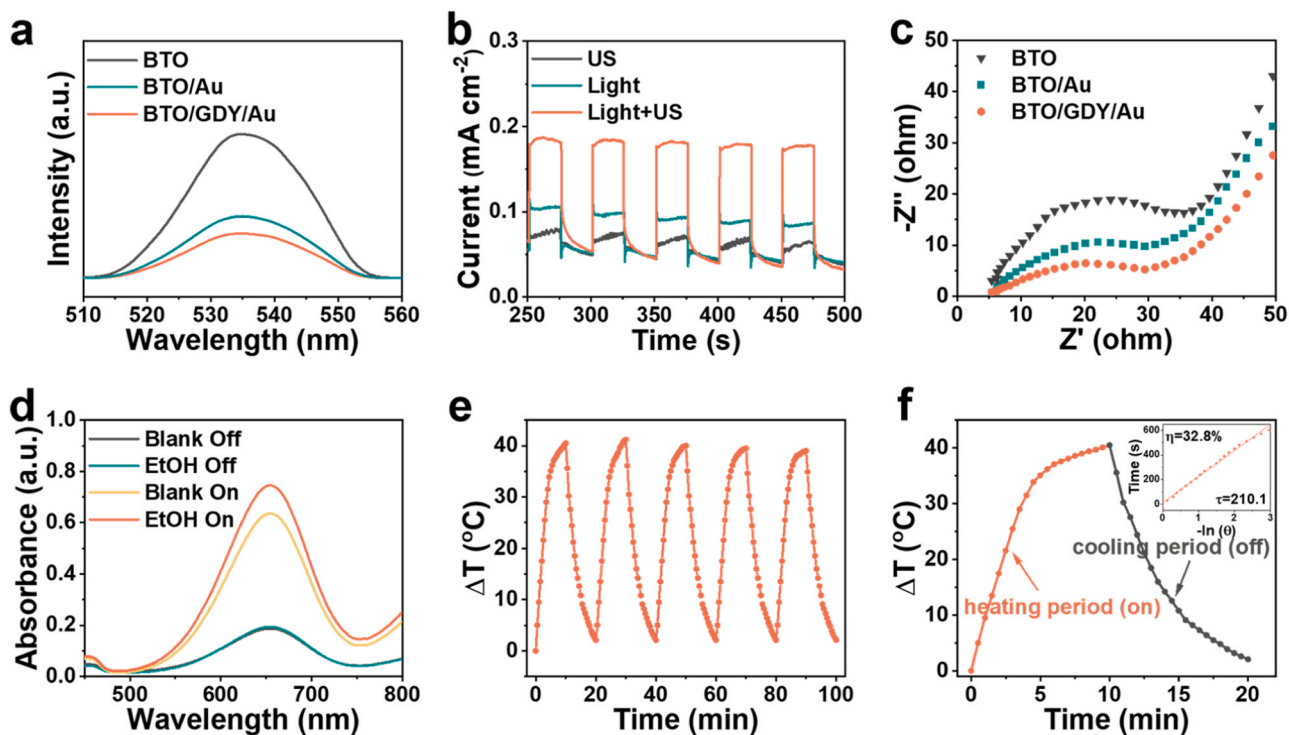
$$d_{33} = (A - A_0)/(V - V_0) \qquad (3)$$

As a result, the d_{33} value of BTO/GDY/Au NFs (127.3 pm/V) is higher than those of BTO/GDY (117.8 pm/V), BTO/Au (51.6 pm/V), and BTO (49.5 pm/V), indicating that GDY promotes piezoelectric properties.

The UV–vis diffuse reflectance spectra of BTO/GDY/Au NFs were measured. Fig. S6 shows that there were no characteristic absorption peaks for BTO/GDY/Au NFs. Photoluminescence (PL) spectroscopy is used to determine the magnitude of photogenerated electron and hole recombination rates. As depicted in Fig. 3a, the peak of BTO/GDY/Au NFs was lower than that of BTO and BTO/Au, which suggests that BTO/GDY/Au NFs prevent the recombination of photogenerated electrons and holes more efficiently than BTO and BTO/Au. As shown in Fig. 3b and S7, the current response of BTO/GDY/Au NFs under light and ultrasound stimulation was pronouncedly improved, and the saturation current density (0.13 mA/cm^2) was 2.6-fold higher than that under light exposure (0.05 mA/cm^2), indicating that light and ultrasound can contribute to the production of more free electrons from BTO/GDY/Au NFs. Additionally, by examining the current responses under various external field conditions, the current responses associated with the LSPR effect and the piezoelectric effect contribute 38.5% and 14.6% to the overall current response, respectively, highlighting the greater influence of the LSPR effect compared to the piezoelectric effect. Electrochemical impedance spectroscopy (EIS) also demonstrates the dynamics of charge carrier transfer in the interfacial region of BTO/GDY/Au NFs [9]. The relative arc radii of the three nanomaterials are in the order of BTO > BTO/Au > BTO/GDY/Au NFs (Fig. 3c), suggesting a better conductivity and a higher interfacial charge carrier transfer efficiency exhibited by BTO/GDY/Au NFs. The LSPR effect was verified to produce hot electrons using ethanol (EtOH) as a hole scavenger [62]. The addition of EtOH had no significant effect when there was no light, whereas it further improved the catalytic activity under light exposure (Fig. 3d). This result indicated that hot electrons and holes were generated in Au NPs under light, and some hot holes are scavenged by EtOH, leaving more hot electrons.

The investigation focused on elucidating the impact of photothermal effect on the catalytic activity of the heterostructure. Upon 10 min of light exposure, the temperature of the system increased by approximately 40 °C when the concentration reached 200 μg mL^{-1}, whereas the control ultrapure water exhibited negligible change (Figs. S8, S9). The sustainability of the photothermal conversion process was investigated, demonstrating that the generated heat did not diminish significantly over five consecutive switching cycles (Fig. 3e). The photothermal conversion efficiency of BTO/GDY/Au NFs was quantified as 32.8%, (Fig. 3f) suggesting that the photothermal effect cannot take on critical significance in the catalytic process. Furthermore, the influence of wavelength on the photothermal effect was investigated. The results show that lower wavelengths of light have a better photothermal effect than higher wavelengths of light when irradiated, indicating a wavelength-dependent photothermal effect (Figs. S10, 11). The effect of catalytic activity of BTO/GDY/Au NFs under different temperature and light conditions was determined (Fig. S12), implying that both light and elevated temperatures can enhance the catalytic activity. In addition, the light-induced hot electron effect and photothermal effect were quantified through i-t curves (Fig. S13), where the contribution of the hot electron effect is expressed as $(i_1 - i_0)/i_1$ [63]. The results indicate that the hot electron effect leads to a more significant increase in current density at 55 °C compared to 15 °C after light irradiation, with a contribution ratio of 48.4% at 55 °C and 23.6% at 15 °C. All these findings collectively establish that both photothermal effect and hot electron effect contribute to enhancing the catalytic activity of BTO/GDY/Au NFs.

Fig. 3. (a) PL spectra of BTO NFs, BTO/Au, and BTO/GDY/Au NFs. (b) Piezoelectric and photocurrent response of BTO/GDY/Au NFs. (c) EIS spectra of BTO, BTO/Au, and BTO/GDY/Au NFs. (d) UV–vis spectra of TMBox with and without EtOH with and without LSPR excitation. (e) Photothermal stability (five light on/off cycles). (f) Determination of photothermal conversion efficiency (η) of BTO/GDY/Au NFs.
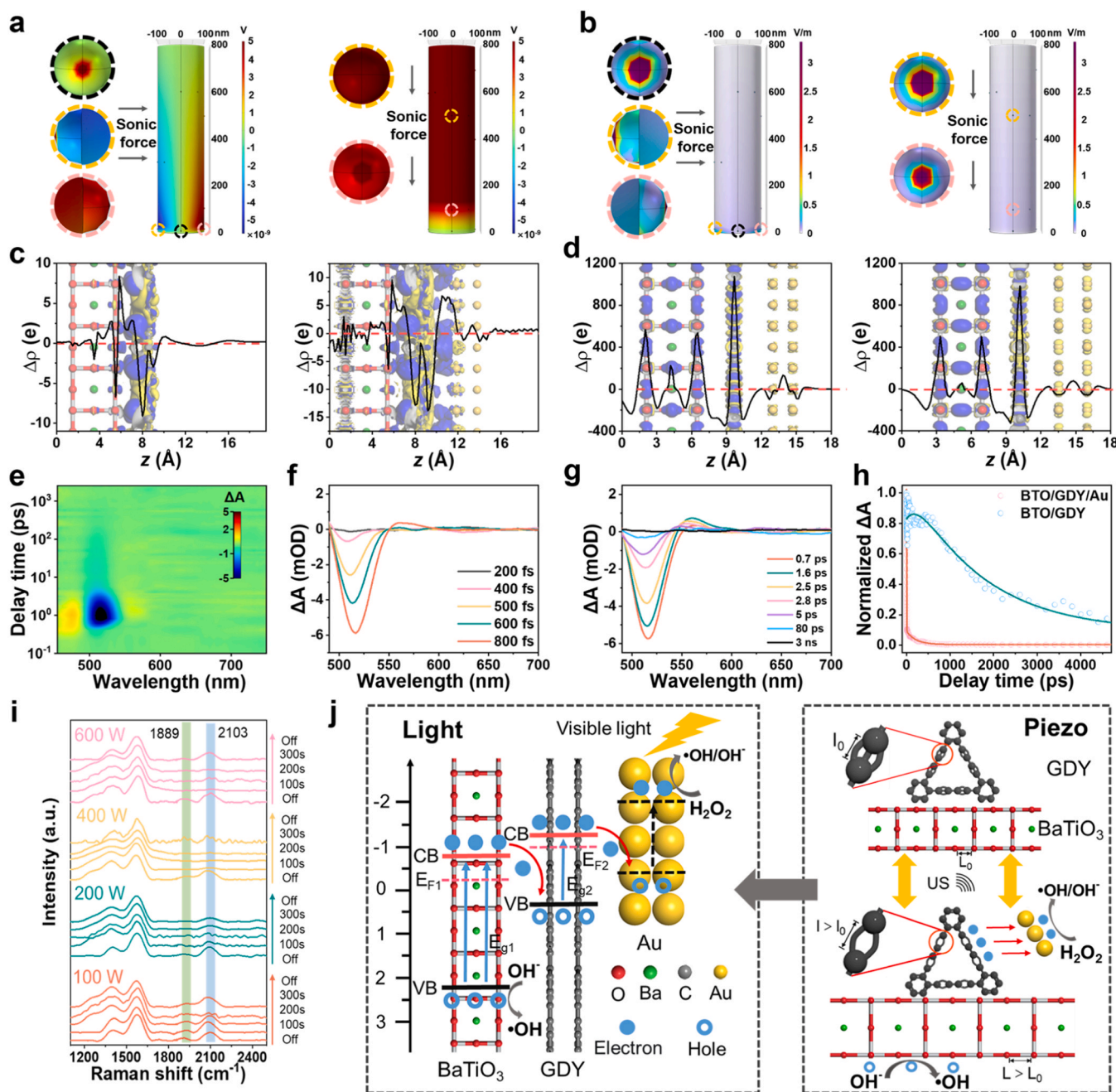
3.3. Piezoelectric-enhanced photocatalytic mechanism of BTO/GDY/Au NFs

In this work, it is found that the piezoelectric effect can improve the photocatalytic performance of BTO/GDY/Au NFs. It is assumed that BTO/GDY can release electrons under ultrasound to enhance the LSPR of Au NPs. To verify this speculation, modeling calculations on the materials (Fig. S14) as a way to probe the catalytic mechanism of BTO/GDY/Au NFs.

The electric field strengths at different positions of the BTO/GDY/Au NFs were calculated when irradiated under different wavelengths of the light (from 290 nm to 900 nm) (Fig. S15). At any wavelength, the surface of Au NPs and the aqueous environment present a stronger positive electric field than BTO and GDY, which attracts electrons toward to the surface of Au NPs (Fig. S16). Compared with BTO/Au, the BTO/GDY/Au NFs exhibit a negative electric field at GDY when exposed to light at wavelengths greater than 600 nm, which further promotes the transfer of electrons from GDY to Au NPs.

Next, the investigation aimed to explore the piezoelectric effect on BTO/GDY/Au NFs. When mechanical forces of varying directions were applied to the BTO/GDY/Au NFs, different magnitudes of stresses were exerted on different positions of the BTO/GDY/Au NFs, resulting in the

Fig. 4. Catalytic mechanisms of BTO/GDY/Au NFs. (a) Electric field maps of BTO/GDY/Au NFs in light and x- and z-axis ultrasound fields. (b) Plot of electric field strength of BTO/GDY/Au NFs under illumination and x- and z-axis ultrasound fields. (c) Electron density difference plots for BTO/GDY, and BTO/GDY/Au NFs and z-axis values of electron density difference. (d) Electron density difference plots of BTO/GDY/Au NFs in stretching (left) or compression (right), where positive and negative values represent electron gains and losses. Pseudocolor plots (e) and fs-TAS spectra (f, g) of BTO/GDY/Au NFs under 400 nm laser pulse excitation. (h) Normalized decay kinetic curves at 500 nm of BTO/GDY and BTO/GDY/Au NFs. (i) In situ Raman profiles of BTO/GDY/Au NFs at different ultrasound powers over time. (j) Charge transfer pathways of BTO/GDY/Au NFs under light and ultrasound and their possible catalytic mechanisms.

deformation and polarization of BTO/GDY/Au NFs (Fig. S17). Fig. 4a illustrates the surface potential distribution of BTO/GDY/Au NFs when subjected to light radiation and mechanical forces in different directions, where electrons move from low to high potentials during the catalytic reaction. When the BTO/GDY/Au NFs were subjected to mechanical forces in different directions, the potential on the surface of Au NPs exceeded that at GDY, indicating that the electrons can move from GDY to Au NPs. The influence of piezoelectric effect on the surface potential of BTO/GDY/Au NFs was investigated (Fig. S18). Noteworthily, no significant was reported difference between the potentials of Au NPs and GDY, suggesting that electron transfer does not occur. The electric field film represents the magnitude of the electric field intensity at each of the BTO/GDY/Au NFs, with a higher electric field strength indicating a greater electron enrichment here. When only ultrasound was applied, the portion of the electric field intensity greater than zero was primarily distributed at the junction of the Au NPs and the GDY. The electric field intensity on the surface of Au NPs exceeded zero under both light and ultrasound exposure (Fig. 4b), where the electric field intensity the largest at the tip of Au NPs, indicating that this region is more favorable for the occurrence of the catalytic reaction.

In addition, the stress distribution on BTO/GDY/Au NFs in aqueous environments was simulated (Fig. S19). The BTO/GDY/Au NFs were subjected to different magnitudes of stresses at each place, which created conditions for the occurrence of polarization phenomena. We simulated the temperature change of BTO/GDY/Au NFs when irradiated by light in aqueous environment (Fig. S20), and the temperature on the surface of the material would be slightly higher than that inside the material, whereas the temperature change was not significant. Thus, the photothermal effect could not be dominant in the catalytic process, aligning with the above-mentioned results of the photothermal conversion efficiency.

Fig. S14b illustrates the atomic model of BTO/GDY/Au NFs and calculates the electronic and structural changes of BYO/GDY and BTO/GDY/Au NFs models under light and ultrasound. We computed the lattice constants, energies, and structural correspondences of the GDY proto-packages and BTO proto-packages. In the presence of 7.1–10.4 Å equivalent values of GDY proto-packages (Fig. S21a), the magnitude of the a, b values of the lattice of the GDY proto-packages can be stabilized, the difference of the fluctuating energy of the changes was nearly 114.4 eV, and the chemical bonds in the GDY can be kept in the stable state. In contrast, the chemical bonds would be damaged and could not be restored to the stable state. In the presence of 2.6–4.4 Å equivalents, the a, b, and c values of the BTO protocell lattice could be stabilized with a difference of nearly 152.6 eV in the variation energy fluctuations (Fig. S21b).

The most stable structures of GDY and BTO were utilized for layer stacking. Subsequently, a surface junction model of a GDY-coated BTO structure was established, and the model underwent structural optimization using the PBE method within the CASTEP module GGA. The electron density difference (EDD) of the optimized model was then calculated. The electron density difference along the z-axis direction in Fig. 4c and S22a regions demonstrated electron enrichment at the GDY and BTO junction. This enrichment resulted in a significant number of holes in the outer layer of BTO, providing favorable conditions for subsequent catalytic reactions involving vacancies on the BTO surface. Subsequently, simulated Au NPs were loaded onto the side of GDY, away from BTO. The model structure was optimized, and the electron density difference was calculated once again. Upon loading Au NPs, the electron cloud arrangement between GDY and BTO exhibited minimal effects. However, it led to an increase in the number of electrons and holes on the GDY side, away from BTO. This phenomenon enabled GDY to potentially receive excess electrons from BTO within a lattice range of approximately 8.5–10.0 Å along the z-axis (Fig. 4c and S22b). Furthermore, the electronic arrangement of the inner layer of BTO became disordered after Au NP loading, resulting in increased energy for both the BTO and GDY layers. Upon the application of ultrasound, the lattice

constants of GDY and BTO experienced either expansion or contraction, deviating from their energy minimum states. Consequently, their internal energy was consumed to restore them to a steady state. When ultrasound stretched or compressed the BTO and GDY (Fig. 4d and S22c, d), more free electrons appeared between the layers of Au NPs. This increased the likelihood of exciting these electrons to generate hot electrons upon illumination. The projected density of states (pDOS) for GDY, BTO, and Au NPs was calculated using density functional theory (DFT). The hot electrons generated by Au NPs upon illumination originated from the outermost d-orbitals of the gold atoms, with energy peaks ranging from −8 to 0 eV. In contrast, GDY and BTO exhibited no or very few energy peaks for d-orbital electrons of similar energies. Thus, it can be observed that the addition of GDY does not increase the number of excited photogenerated electrons but rather reduces their energy levels (Fig. S23).

Femtosecond transient absorption spectroscopy (fs-TAS) was performed to explore the charge carrier transfer process in BTO/GDY/Au NFs (Fig. 4e and S24). Upon excitation with a pump pulse at a wavelength of 400 nm, both BTO/GDY and BTO/GDY/Au NFs exhibited signal bleaching centered at 520 nm (Fig. 4f, g). The kinetic mechanism of charge carrier transfer in BTO/GDY and BTO/GDY/Au NFs was analyzed using the bleaching signal at 520 nm as a reference. The fitting results of normalized decay kinetic curves are presented in Fig. 4h. The decay curves of BTO/GDY and BTO/GDY/Au NFs adhere to a triple exponential function, with three lifetimes on different time scales (Tab. S2). All three lifetimes ($\tau_1 \approx 2.0$ ps, $\tau_2 \approx 2.0$ ps, and $\tau_3 \approx 218.8$ ps) of the BTO/GDY/Au NFs were reduced compared to the BTO/GDY ($\tau_1 \approx 268.1$ ps, $\tau_2 \approx 1668.2$ ps, and $\tau_3 \approx 268.1$ ps), indicating the transfer of electrons from GDY to Au NPs. Additionally, the τ_{ave} after loading Au NPs decreased from 1611.1 ps to 186.7 ps, further confirming the occurrence of electron transfer at the interface of BTO/GDY and Au NPs.

A key factor in evaluating redox capacity is the edge potentials of the conduction band (CB) and valence band (VB). Both BTO and GDY showed significant uptake in the visible region (Figs. S25a, c). Bandgaps of 2.90 and 1.55 eV for BTO and GDY were determined from the Tauc plots (Figs. S25b, d). Depending on the forbidden bandwidth, the VB and CB edge potentials were 2.15 and −0.75 eV for BTO and 0.33 and −1.22 eV for GDY, respectively (Fig. S26). When BTO and GDY came into contact to form a Z-scheme heterojunction, electrons flowed from the BTO to the GDY. Due to the different Fermi energy levels of GDY and Au NPs, the charge carriers at the interface of GDY and Au NPs were redistributed, resulting in the diffusion of electrons from GDY to Au NPs. When light was irradiated onto the BTO/GDY/Au NFs, electrons and holes were formed on the VB and CB of the BTO and GDY, respectively, and the electrons on the CB of the BTO were transferred to the VB of the GDY to complex with the holes, and the net positive charge left in the BTO is used to reduce OH^- to $\bullet OH$ (Fig. 4f). Under the LSPR effect, Au NPs can produce considerable hot electron-hole pairs under light irradiation, and the difference in Fermi energy levels can cause the electrons of CB on GDY to be transferred to the electron cloud around the Au NPs to complex with hot holes. Therefore, Au NPs can serve as active sites to catalyze the decomposition of H_2O_2 into OH^- and $\bullet OH$, thus improving the catalytic activity of BTO/GDY/Au NFs.

Due to the presence of a large significant of C≡C in GDY, the conversion of C≡C to C=C may occur under simultaneous exposure to light and ultrasound, resulting in the release of electrons that enhance catalytic activity. To validate this hypothesis, in situ Raman spectroscopy was employed to investigate the changes in chemical bonding during the reaction of BTO/GDY/Au NFs (Fig. 4e) [64,65]. The peaks observed at around 1889 and 2103 cm^{-1} were attributed to the vibration of diyne links (C≡C-C≡C) and certain vibrations associated with C≡C. Under the influence of the ultrasound field, the intensity of the peak at 2103 cm^{-1} was observed to weaken, indicating the conversion of a certain proportion of C≡C in GDY to C=C due to stretching or

compression induced by BTO. The corresponding lattice constants ranged from 7.1 to 10.4 Å. Throughout the reaction, only the chemical bonds of BTO/GDY/Au NFs experienced changes while remaining in a stable state. This observation aligns with the stability experiments mentioned, earlier and further confirms the stability of BTO/GDY/Au NFs. In situ Raman profiles were examined under different ultrasound power levels, revealing that the intensity of the peaks associated with C≡C decreased as the ultrasound power increased. This trend suggests a higher conversion of C≡C to C=C. Based on these findings, a possible mechanism for piezoelectric catalysis was proposed. When BTO/GDY/Au NFs are subjected to ultrasound, mechanical vibrations occur. As the Ti-O bond in BTO stretches due to the ultrasound effect, the electron cloud density decreases, leading to the generation of more holes that oxidize OH⁻ to •OH. Simultaneously, C≡C in GDY convert to C=C, and the overall lattice constant increases, facilitating the reception of electrons from the CB of BTO. Conversely, when the Ti-O bond in BTO is compressed by ultrasound, the electron cloud density around BTO increases, causing electron transfer to GDY. Consequently, C≡C in GDY convert to C=C, resulting in a smaller the overall lattice constant and the generation of excess electrons. This elevated electron cloud density around the Au NPs enhances the likelihood of exciting surface electrons upon light irradiation, thereby promoting the decomposition of H_2O_2. In summary, the generated hot electrons and holes possess strong reducing and oxidizing abilities, enabling them to react with H_2O_2 in the solution,

leading to the production of a large number of reactive oxygen radicals. The specific reaction pathway is by the following equations:

$$BTO/GDY/Au\ NFs + Light + US \rightarrow BTO/GDY/Au\ NFs(e^- + h^+) \quad (4)$$

$$H_2O_2 + e^- \rightarrow OH^- + \bullet OH \quad (5)$$

$$O_2 + e^- \rightarrow \bullet O_2^- \quad (6)$$

$$OH^- + h^+ \rightarrow \bullet OH \quad (7)$$

$$\bullet O_2^- + \bullet OH \rightarrow OH^- + {}^1O_2 \quad (8)$$

3.4. Piezoelectric-enhanced photocatalytic degradation of dyes and antibiotics by BTO/GDY/Au NFs

The present study employed a heterostructure of piezoelectric-enhanced photocatalysis for the degradation of a model wastewater containing MB, which was monitored by observing the decrease in its absorbance peak at 663 nm (Fig. 5a). The results demonstrated that the degradation efficiency of MB in the BTO/GDY/Au NFs + H_2O_2 experimental group after simultaneous application of light and ultrasound for 30 min, was significantly higher compared with when only light was applied (Fig. 5b). In the remaining groups, the degradation rate of MB was negligible. The first kinetic constant for the catalytic degradation of MB by BTO/GDY/Au NFs in the presence of light and ultrasound was
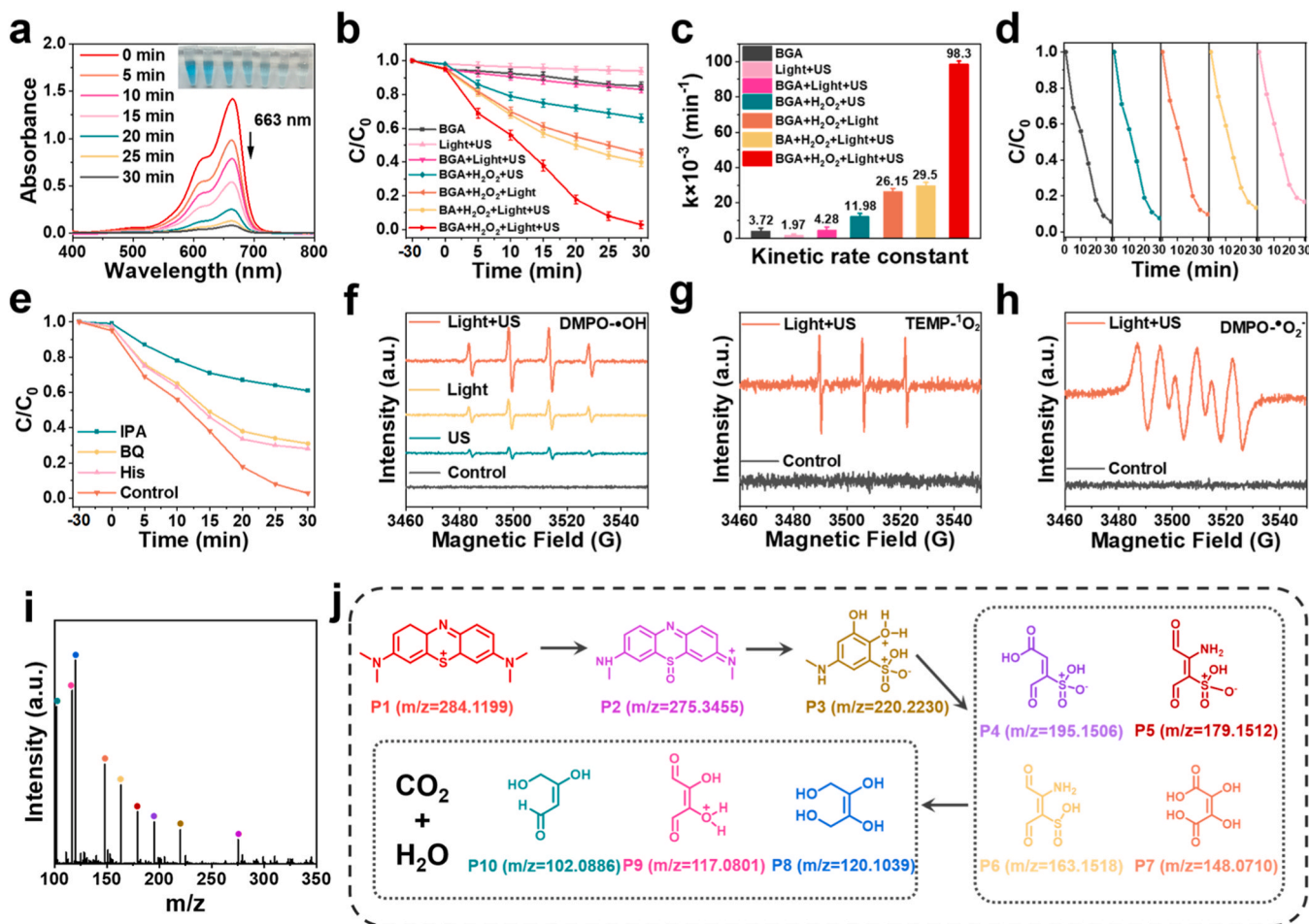

Fig. 5. Degradation of methylene blue (MB) by BTO/GDY/Au NFs (BGA). (a) UV-Vis spectra of MB degradation processes. (b) Degradation of MB under different conditions. (c) Kinetics of MB degradation under different scenarios. (d) Free radical scavenging experiments. (f-h) EPR spectra of DMPO-•OH adducts, TEMP-1O2 adducts, and DMPO-•O2-. [DMPO]=[TEMP]=50 mM. (i) Digital pictures of different types of simulated wastewater before and after degradation. (j) Antimicrobial behavior of domestic sewage, seawater, river water and industrial wastewater.

determined to be 98.3 min^{-1}, which was 3.8-fold higher than the first kinetic constant in the presence of light alone, and considerably larger than that of the other control groups (Fig. 5c). Notably, the first kinetic constant of BTO/GDY/Au NFs was 3.3-fold higher than that of BTO/Au, further underscoring the enhanced catalytic activity imparted by GDY. These findings indicate that the resulting catalysts possess a strong capability to degrade dyes, benefiting from the synergistic effects of the piezoelectric effect and photocatalysis [66]. In comparison to other piezo-photocatalytic materials, the BTO/GDY/Au NFs exhibited excellent competitiveness (Tab. S3). Furthermore, the recycling performance of BTO/GDY/Au NFs was investigated, revealing no significant decrease in the degradation capacity after five cycles (Fig. 5d).

The degradation mechanism of MB by BTO/GDY/Au NFs was analyzed through active substance capture experiments. Isopropyl alcohol (IPA), 1,4-benzoquinone (BQ), and L-histidine (His) served as scavengers of ●OH, ●O$_2^-$ and ^{1}O$_2$, respectively, to determine the type of active radicals. When ●OH was captured by IPA, the degradation efficiency of MB decreased by 58.2%. In the presence of BQ and His, the removal of MB decreased from 97.2% to 69.0% and 71.9%, respectively, indicating that ●OH, ●O$_2^-$, and ^{1}O$_2$ can play a certain role in the degradation of MB (Fig. 5e). In addition, the types of free radicals produced during degradation were further tested by electron paramagnetic resonance (EPR). 5,5-Dimethyl-1-pyrroline N-oxide (DMPO) and 2,2,6,6-tetramethylpiperidine (TEMP) served as spin trapping agents to capture ●OH, ^{1}O$_2$ and ●O$_2^-$. In the absence of any external field, weak radical signals were detected in the reaction system. Besides, we detected strong characteristic signals of DMPO-●OH (1:2:2:1), TEMP-^{1}O$_2$ (1:1:1) and DMPO-●O$_2^-$ (1:1:1:1) under light and ultrasound exposure (Fig. 5f-h). Notably, the peak intensity of DMPO-●OH exhibited in the presence of

light and ultrasound was much larger than that in light, suggesting that ultrasound promoted the production of more ●OH in the photocatalytic system, further illustrating the promotion of photocatalysis by piezoelectric effect. Fig. S27 demonstrates the EPR spectra of trapped holes, where when the BTO/GDY/Au NFs were subjected to light and ultrasound radiation, a built-in electric field was generated internally, thus inhibiting the recombination of electrons and holes and further leading to an increase in holes within the reaction system.

To investigate the degradation mechanism, high-resolution electrospray ionization mass spectrometry (HR-ESI-MS) was employed to monitor the intermediates formed during the degradation of MB [67]. Pure MB was first subjected to mass spectrometry analysis (Fig. S28), revealing a prominent peak at *m/z* 284.1199, corresponding to the molecular ion peak of MB. Subsequent mass spectrometry analysis of the degraded solution (Fig. 5i) revealed the complete disappearance of the main peak at m/z 284.1199, indicating the thorough degradation of the MB molecule. Moreover, nine new species were identified with *m/z* of 275.3455, 220.2230, 195.1506, 179.1512, 163.1518, 148.0710, 120.1039, 117.0801, and 102.0886. These values correspond to C$_{14}$H$_{14}$N$_3$SO, C$_7$H$_{10}$NSO$_5$, C$_4$H$_5$NSO$_6$, C$_4$H$_5$NSO$_5$, C$_4$H$_5$NSO$_4$, C$_4$H$_4$O$_6$, C$_4$H$_8$O$_4$, C$_4$H$_5$O$_4$, and C$_4$H$_6$O$_3$, suggesting that smaller intermediates were produced by disrupting the chemical structure in the MB during degradation. Notably, the peak intensities of 120.1039, 117.0801 and 102.0886 were higher than compared with the other detected species, indicating that these compounds likely represent the final products. Consequently, a possible MB degradation pathway was proposed (Fig. 5j), involving the degradation of the chromophore, demethylation, deamination and ring opening processes.

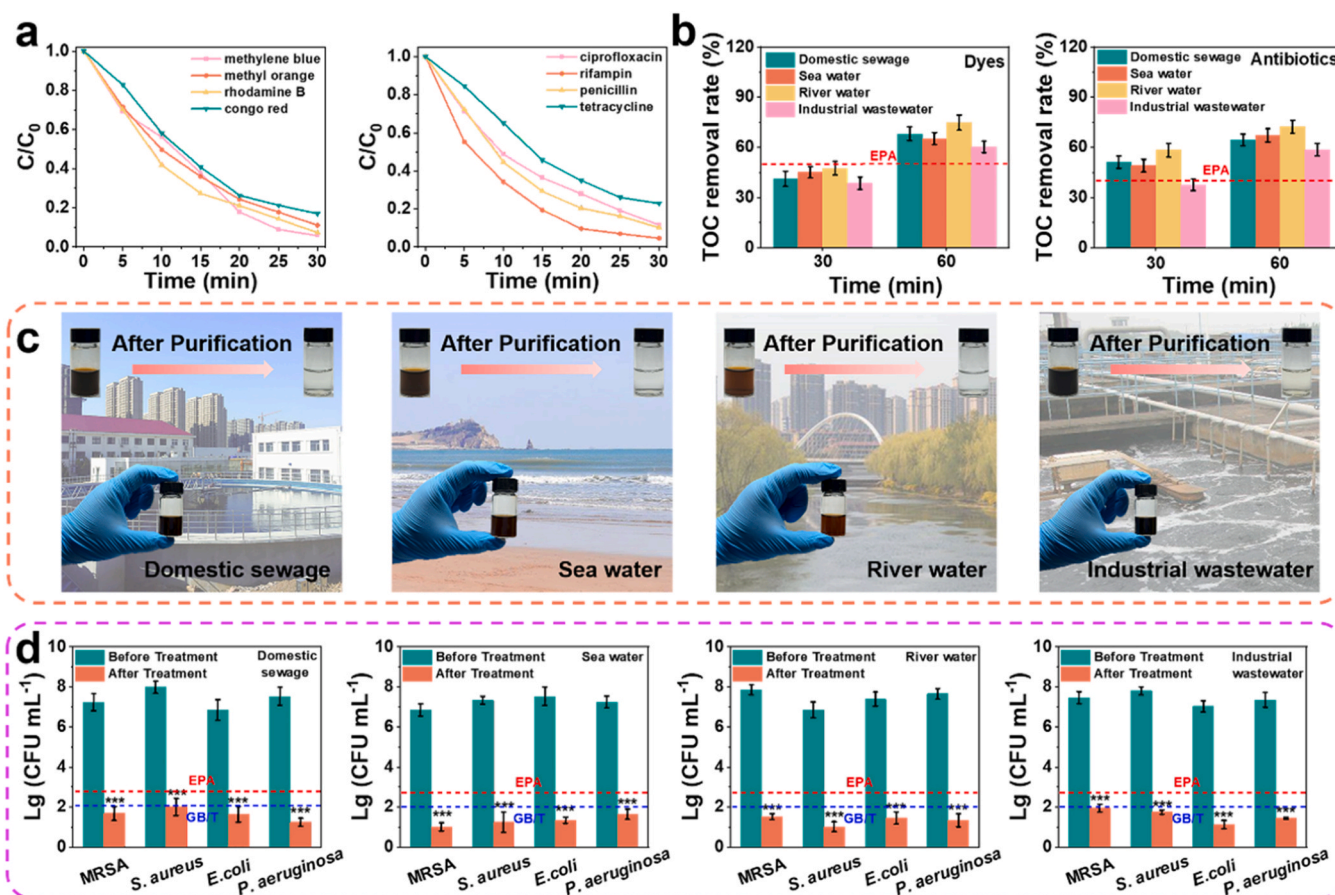The capacity of BTO/GDY/Au NFs for the broad-spectrum

Fig. 6. BTO/GDY/Au NFs degradation of pollutants in water bodies. (a) Degradation behavior of different dyes and antibiotics. (b) TOC removal in simulated dye wastewater and simulated pharmaceutical wastewater. (c) Digital pictures of different types of simulated wastewater before and after degradation. (d) Antimicrobial behavior of domestic sewage, seawater, river water and industrial wastewater.

degradation of wastewater was investigated, focusing on the degradation of four dyes and antibiotics. The degradation rates of MB, MO, Rh B, and Congo red reached 94.2%, 88.9%, 92.6%, and 83.0%, respectively, and those of ciprofloxacin, rifampicin, penicillin, and tetracycline determined as 88.4%, 95.4%, 90.2%, and 77.0%, respectively (Fig. 6a and S29, S30). These findings demonstrate the remarkable efficacy of BTO/GDY/Au NFs in effectively degrading various dyes and antibiotics with distinct chemical structures, underscoring its immense potential for practical application.

Total Organic Carbon (TOC) is a crucial indicator used to evaluate the presence of organic pollutants in wastewater samples and the quality of treated water. In the case of simulated wastewater containing dyes and drugs, the removal of TOC from the simulated dye- and drug-containing wastewater reached levels of 60–75% and 58–72%, respectively, after 60 min of treatment (Fig. 6b). These removal rates surpassed the drinking water quality standards issued by the U.S. Environmental Protection Agency (EPA). Fig. 6c presents contaminated river water, sea water, industrial wastewater and domestic sewage wastewater before and after treatment, all kinds of contaminated wastewater exhibited a remarkable transformation, resulting in clear and transparent water after treatment.

Meanwhile, bacterial disinfection experiments were carried out on domestic sewage, seawater, river water and industrial wastewater (Fig. 6d). The colony count of MRSA after seawater treatment was 6.83 orders of magnitude lower than that before treatment, equivalent to 99.9999%, and the colony count of MRSA after industrial wastewater treatment was 5.51 orders of magnitude lower than that before treatment, equivalent to 99.999%, which were higher than that of the drinking water quality standards published by China (GB/T) and the United States (EPA). These results indicate that BTO/GDY/Au NFs are capable of degrading specific pollutants and pathogen sterilization in a variety of wastewaters.

The efficient removal of MB by BTO/GDY/Au NFs prompted us to further investigate their potential application at the device level. Fig. 7a, b illustrates the wastewater treatment flow chart and digital images, respectively, of the wastewater treatment unit for BTO/GDY/Au NFs in practical applications. To evaluate the degradation performance of BTO/GDY/Au NFs, samples were collected from the secondary effluent of Tuandao wastewater treatment plant (Qingdao, China). The MB was introduced into the secondary effluent as an indicator of organic matter removal. The long-term stability was evaluated through continuous operation for over 300 min. The BTO/GDY/Au NFs system continuously removes contaminants from wastewater without the need to add catalyst after a single reaction. As depicted in Fig. 7c, the BTO/GDY/Au NFs system exhibited continuous removal of contaminants from wastewater, maintaining a high MB removal efficiency of 95.4% after 300 min continuous operation. Fig. S31 depicts representative images of wastewater treatment at various intervals. Another advantage of the system was its ability to achieve satisfactory TOC removal rates after 300 min operation (Fig. 7d). This indicates that the BTO/GDY/Au NFs can maintain a high concentration of radical generation. The aforementioned discussion highlights the broad range of practical applications of BTO/GDY/Au NFs in wastewater treatment scenarios.

3.5. Antimicrobial activity studies of BTO/GDY/Au NFs

The antimicrobial activity of BTO/GDY/Au NFs was evaluated by using MRSA and *E. coli* (Fig. 8a, b). Controls involving buffer or H_2O_2 alone, with or without an external field, exhibited negligible antimicrobial activity, and the corresponding LB agar plates were completely covered with colonies. In the control group treated with BTO/GDY/Au NFs, a reduction in the number of colonies was observed compared with the blank group, which was further diminished under light and ultrasound treatments. In contrast, the BTO/GDY/Au NFs + H_2O_2 experimental group displayed the most effective bactericidal performance under light and ultrasound conditions, with no colonies detected on LB
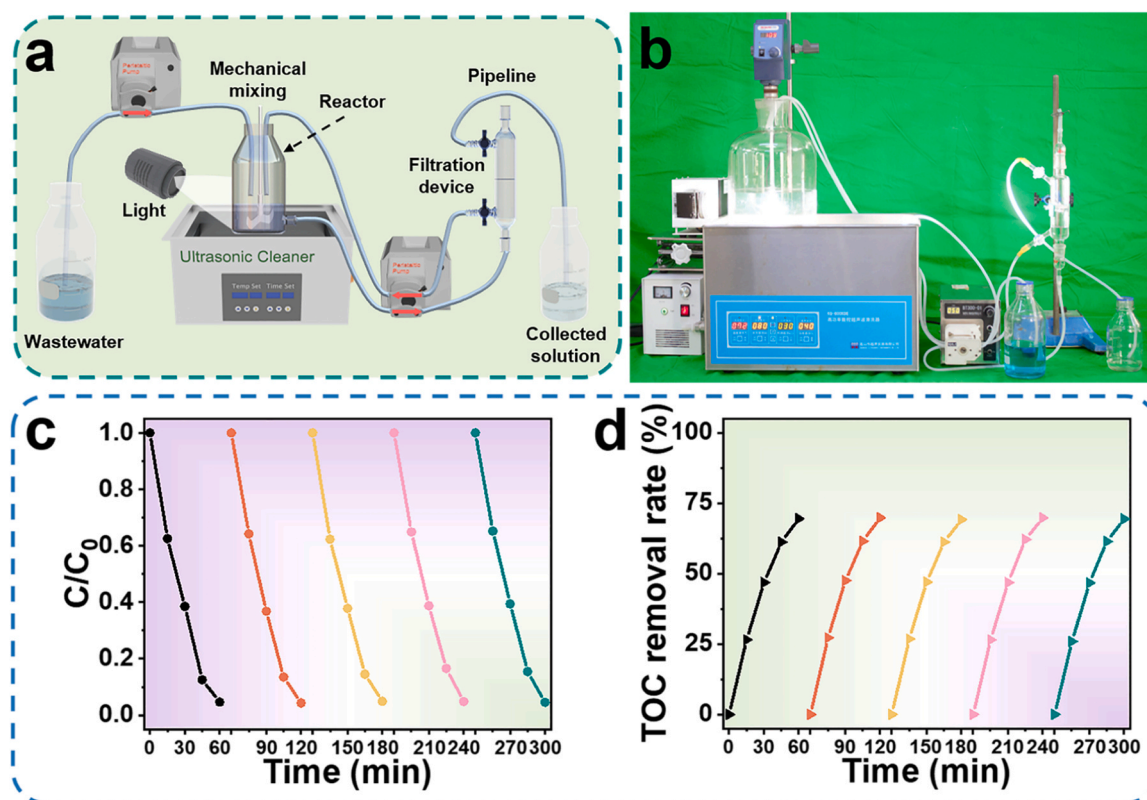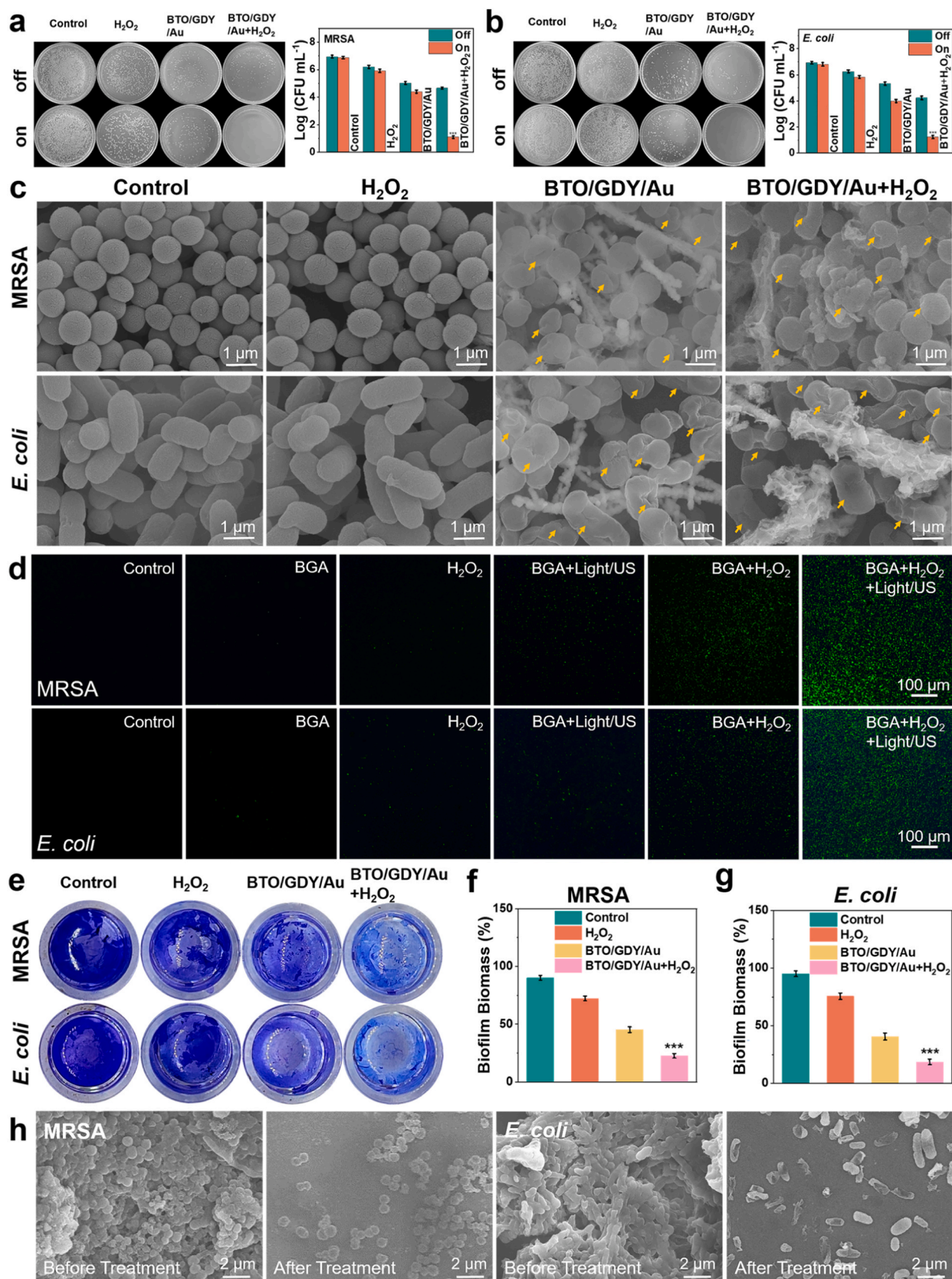

Fig. 7. Application of BTO/GDY/Au NFs for wastewater treatment. (a) Schematic diagram of a continuous wastewater treatment ennent reactor. (b) The laboratory-scale setup of the continuous wastewater treatment reactor. (c) MB degradation rate as a function of time. (d) TOC removal rate during continuous reaction.

Fig. 8. Antimicrobial properties of BTO/GDY/Au NFs. (a) Digital pictures of MRSA colonies and counts of colonies under different treatments. (b) Digital pictures of *E. coli* colonies and counts of colonies under different treatments. (c) SEM images of MRSA and *E. coli* under different treatments. Yellow arrows represent typical deformations of bacterial morphology. (d) Fluorescence images of MRSA and *E. coli* after various treatments using the DCFH-DA probe. (e-g) Crystalline violet staining of MRSA and *E. coli* biofilms after different treatments. (h) SEM images of MRSA and *E. coli* biofilms before and after treatment. Values are mean $\pm$ S.D., n = 3. * $p < 0.05$, ** $p < 0.01$, and *** $p < 0.001$.

agar plates, indicating near-complete eradication of bacteria. Quantitative comparison of bacterial survival through plate counting confirmed the superior bactericidal effect of the BTO/GDY/Au NFs + H_2O_2 experimental group under light and ultrasound exposure. The number of colonies of MRSA and *E. coli* by 5.93 and 5.71 orders of magnitude, respectively, corresponding to bacterial killing rates greater than 99.999%. This remarkable bactericidal effect can be attributed to the bacterial death caused by the disruption of the bacterial cell membrane due to considerable reactive ROS generated by BTO/GDY/Au NFs and H_2O_2 under of light and ultrasound exposure. The minimum inhibitory concentration for 50% of the bacterial population (MIC_{50}) for BTO/GDY/Au NFs to kill 50% of the bacterial community population was measured (Fig. S32) and compared with the minimum inhibitory concentrations of the other catalysts. Noteworthily, the MIC_{50} for MRSA and *E. coli* reached 43 ± 1 µg mL^{-1} and 32 ± 1 µg mL^{-1}, respectively, surpassing the reported catalysts, particularly considering due to the short reaction time of only 5 min (Tab. S4).

We performed field emission scanning electron microscopy (FE-SEM) to observe the nano/micro-morphological changes in the bacteria of MRSA and *E. coli* treated with BTO/GDY/Au NFs + H_2O_2. The surfaces of bacteria in the blank and H_2O_2 control groups were smooth, whereas the surfaces of bacteria treated with BTO/GDY/Au NFs became pronouncedly rough, and some of the bacteria were severely damaged (Fig. 8c). The above results indicated that ROS generated by the catalyzed reaction disrupted the bacterial cell membranes leading to bacterial death. Moreover, changes in intracellular ROS levels were examined in MRSA and *E. coli* under different conditions. The highest intracellular ROS levels were observed under simultaneous irradiation with light and ultrasound compared with the control (Fig. 8d and S33). In vitro ROS scavenging experiments were performed to demonstrate the type of ROS generated by BTO/GAY/Au NFs + H_2O_2 in the LSPR/piezoelectric system. The bacterial survival rates after the addition of IPA, BQ, and His were determined as 89%, 5%, and 2% (Fig. S34), indicating •OH as the main product of the decomposition of H_2O_2 by BTO/GAY/Au NFs in the presence of light and ultrasound. Furthermore, in vitro antimicrobial bacterial biofilm studies were conducted by employing MRSA and *E. coli*. The anti-biofilm effect of BTO/GDY/Au NFs was investigated through crystal violet staining (determination of OD at 570 nm) (Fig. 8e). Most of the biofilms in control, H_2O_2 and BTO/GDY/Au NFs groups remained alive and intact. Nevertheless, the biofilms in the BTO/GDY/Au NFs + H_2O_2 group exhibited a significant disruption, and a simple quantitative analysis indicated that the residual biofilms of MRSA and *E. coli* in the BTO/GDY/Au NFs + H_2O_2 group were only 22.6% and 18.5% (Fig. 8f, g), proving the significant inhibitory effect of BTO/GDY/Au NFs on biofilm. In addition, biofilms cultivated on wafers were examined using SEM (Fig. 8h). In the absence of treatment, *E. coli* and MRSA bacteria formed biofilms. After treatment with BTO/GDY/Au NFs + H_2O_2, no bacterial biofilm was observed, and more areas showed attachment of single cells only. In brief, the possible mechanisms of sterilization by BTO/GDY/Au NFs are elucidated as follows. (1) BTO/GDY/Au NFs can contribute to the decomposition of H_2O_2 under light and ultrasound to produce a large amount of •OH, inducing the oxidative stress of bacteria. (2) BTO/GDY/Au NFs adsorb on the surface of the bacteria, thus disrupting the cell membranes and inducing bacterial death.

4. Conclusions

A three-phase heterostructure comprising BTO/GDY/Au NFs was synthesized, demonstrating enhanced piezo-photocatalytic activity. The insertion of a layer of GDY between BTO and Au resulted in a 3.3-fold increase in the degradation rate constant, highlighting the role of GDY as an electron sponge. The ultrasound-induced stretching or compression of BTO led to corresponding changes in GDY lattice constants within the range of 7.1–10.4 Å. This resulted in the reversible conversion of the sp-hybridized C≡C to C=C in GDY, facilitating the release of electrons. The above-mentioned electrons transferred to Au NPs and recombined with the generated hot holes, thus enabling more hot electrons to participate in the catalytic reaction, and improving the photocatalytic activity. The BTO/GDY/Au NFs were successfully employed for the degradation of various dyes and antibiotics in wastewater and were effective in eliminating MRSA and *E. coli* with bactericidal efficiencies greater than 99.999%. This study provides valuable insights for the rational design of highly efficient piezo-photocatalysts.

CRediT authorship contribution statement

Ning Sui: Writing – review & editing, Validation, Supervision, Methodology, Investigation, Funding acquisition. **Zhiling Zhu:** Writing – review & editing, Supervision, Investigation, Funding acquisition. **Lina Wang:** Writing – review & editing, Supervision, Funding acquisition. **Qiang Bai:** Writing – review & editing, Supervision, Investigation, Formal analysis, Funding acquisition. **Fuguo Ge:** Formal analysis. **Yujie Jiang:** Investigation, Formal analysis. **Wenbo Feng:** Writing – original draft, Investigation, Formal analysis, Data curation. **Gang Niu:** Writing – review & editing. **Rui Cao:** Formal analysis. **Limin Shang:** Formal analysis. **Jun Yang:** Data curation.

Declaration of Competing Interest

The authors declare that they have no known competing financial interests or personal relationships that could have appeared to influence the work reported in this paper.

Data Availability

No data was used for the research described in the article.

Appendix A. Supporting information

Supplementary data associated with this article can be found in the online version at doi:10.1016/j.apcatb.2024.123868.

References

[1] L. Guo, C. Zhong, J. Cao, Y. Hao, M. Lei, K. Bi, Q. Sun, Z.L. Wang, Enhanced photocatalytic H$_2$ evolution by plasmonic and piezotronic effects based on periodic Al/BaTiO$_3$ heterostructures, Nano Energy 62 (2019) 513–520.

[2] X. Jiang, H. Wang, X. Wang, G. Yuan, Synergetic effect of piezoelectricity and Ag deposition on photocatalytic performance of barium titanate perovskite, Sol. Energy 224 (2021) 455–461.

[3] J. Xu, T. Qin, W. Chen, J. Lv, X. Zeng, J. Sun, J.Zhou Y.-y. Li, Synergizing piezoelectric and plasmonic modulation of Ag/BiFeO$_3$ fibrous heterostructure toward boosted photoelectrochemical energy conversion, Nano Energy 89 (2021) 106317.

[4] Z.L. Wang, Y. Zhang, W. Hu, W, Piezocatalysis and piezophototropic effect on catalysis. Piezotronics and Piezo-Phototronics. Microtechnology and MEMS, Springer,, Cham, 2023, pp. 475–498.

[5] J.M. Wu, W.E. Chang, Y.T. Chang, C.K. Chang, Piezo-catalytic effect on the enhancement of the ultra-high degradation activity in the dark by single-and few-Layers MoS$_2$ nanoflowers, Adv. Mater. 28 (19) (2016) 3718–3725.

[6] Y.-L. Liu, J.M. Wu, Synergistically catalytic activities of BiFeO$_3$/TiO$_2$ core-shell nanocomposites for degradation of organic dye molecule through piezophototronic effect, Nano Energy 56 (2019) 74–81.

[7] J. Yuan, W. Feng, Y. Zhang, J. Xiao, X. Zhang, Y. Wu, W. Ni, H. Huang, W. Dai, Unraveling synergistic effect of defects and piezoelectric field in breakthrough piezo-photocatalytic N$_2$ reduction, Adv. Mater. 36 (5) (2023) 202303845.

[8] W. Liang, Y. Liu, W. Bian, W. Qin, Y. Wang, W. Guo, D. Li, H. Zeng, J. Zhong, Y. Sun, H. Lin, L. Jiang, Cascaded hot electron transfer within plasmonic Ag@Pt heterostructure for enhanced electrochemical reactions, Sci. China Mater. 66 (6) (2023) 2227–2234.

[9] Z. Zhu, H. Luo, T. Wang, C. Zhang, M. Liang, D. Yang, M. Liu, W.W. Yu, Q. Bai, L. Wang, N. Sui, Plasmon-enhanced peroxidase-like activity of nitrogen-doped graphdiyne oxide quantum dots/gold-silver nanocage heterostructures for antimicrobial applications, Chem. Mater. 34 (3) (2022) 1356–1368.

[10] L. Liu, A. Thakur, W. Kar Li, G. Qiu, T. Yang, B. He, Y. Lee, C.-M. Lawrence Wu, Site specific biotinylated antibody functionalized Ag@AuNIs LSPR biosensor for the ultrasensitive detection of exosomal MCT₄, a glioblastoma progression biomarker, Chem. Eng. J. 446 (2022) 137383.

[11] L. Hu, Y. Li, X. Peng, W. Zheng, W. Xu, J. Zhu, L.Y.S. Lee, P.K. Chu, K.-Y. Wong, TiO₂ film supported by vertically aligned gold nanorod superlattice array for enhanced photocatalytic hydrogen evolution, Chem. Eng. J. 417 (2021) 127900.

[12] W. Liang, W. Qin, D. Li, Y. Wang, W. Guo, Y. Bi, Y. Sun, L. Jiang, Localized surface plasmon resonance enhanced electrochemical nitrogen reduction reaction, Appl. Catal. B: Environ. 301 (2022) 120808.

[13] H.-Y. Lin, K.T. Le, P.-H. Chen, J.M. Wu, Systematic investigation of the piezocatalysis-adsorption duality of polymorphic MoS₂ nanoflowers, Appl. Catal. B: Environ. 317 (2022) 121717.

[14] C. Zhang, D. Lei, C. Xie, X. Hang, C. He, H.L. Jiang, Piezo-photocatalysis over metal-organic frameworks: promoting photocatalytic activity by piezoelectric effect, Adv. Mater. 33 (51) (2021) 2106308.

[15] C. Hu, H. Huang, F. Chen, Y. Zhang, H. Yu, T. Ma, Coupling piezocatalysis and photocatalysis in Bi₄NbO₈X (X = Cl, Br) polar single crystals, Adv. Funct. Mater. 30 (7) (2021) 1908168.

[16] M.L. Xu, M. Lu, G.Y. Qin, X.M. Wu, T. Yu, L.N. Zhang, K. Li, X. Cheng, Y.Q. Lan, Piezo-photocatalytic synergy in BiFeO₃@COF Z-scheme heterostructures for high-efficiency overall water splitting, Angew. Chem. Int. Ed. 61 (44) (2022) e202210700.

[17] S. Xu, L. Guo, Q. Sun, Z.L. Wang, Piezotronic effect enhanced plasmonic photocatalysis by Au NPs/BaTiO₃ heterostructures, Adv. Funct. Mater. 29 (13) (2019) 1808737.

[18] P.P. Chen, X. Li, Z. Ren, J. Wu, Y. Li, W. Liu, P. Li, Y. Fu, J. Ma, Enhancing photocatalysis of Ag nanoparticles decorated BaTiO₃ nanofibers through plasmon-induced resonance energy transfer turned by piezoelectric field, Catalysts 12 (9) (2022) 987.

[19] Y. Fu, Z. Ren, L. Guo, X. Li, Y. Li, W. Liu, P. Li, J. Wu, J. Ma, Piezotronics boosted plasmonic localization and hot electron injection of coralline-like Ag/BaTiO₃ nanoarrays for photocatalytic application, J. Mater. Chem. C 9 (37) (2021) 12596–12604.

[20] S. Xu, Z. Liu, M. Zhang, L. Guo, Piezotronics enhanced photocatalytic activities of Ag-BaTiO₃ plasmonic photocatalysts, J. Alloy. Compd. 801 (2019) 483–488.

[21] H. Meng, Z. Chen, Z. Lu, X. Wang, Piezoelectric effect enhanced plasmonic photocatalysis in the Pt/BaTiO₃, heterojunctions, J. Mol. Liq. 369 (2023) 120846.

[22] S. Li, Z. Zhao, M. Liu, X. Liu, W. Huang, S. Sun, Y. Jiang, Y. Liu, J. Zhang, Z. Zhang, Remarkably enhanced photocatalytic performance of Au/AgNbO₃ heterostructures by coupling piezotronic with plasmonic effects, Nano Energy 95 (2022) 107031.

[23] C.-Y. Tu, J.M. Wu, Localized surface plasmon resonance coupling with piezophototronic effect for enhancing hydrogen evolution reaction with Au@MoS₂ nanoflowers, Nano Energy 87 (2021) 106131.

[24] B. Shan, N. Yuan, F. Li, X. Zhao, C. Ji, Z. Li, J. Yu, S. Xu, B. Man, C. Zhang, Plasmonic enhanced piezoelectric photocatalytic performance with PVDF@BT/MoS2/Au by strong piezoelectric functional particle doping, J. Alloy. Compd. 925 (2022) 166695.

[25] F. Li, B. Shan, X. Zhao, C. Ji, Z. Li, J. Yu, S. Xu, Y. Jiao, C. Zhang, B. Man, Plasmonic enhanced piezoelectric photoresponse with flexible PVDF@Ag-ZnO/Au composite nanofiber membranes, Opt. Express 30 (18) (2022) 32509–32527.

[26] L. Liu, J. Hu, Z. Ma, Z. Zhu, B. He, F. Chen, Y. Lu, R. Xu, Y. Zhang, T. Ma, M. Sui, H. Huang, One-dimensional single atom arrays on ferroelectric nanosheets for enhanced CO₂ photoreduction, Nat. Commun. 15 (1) (2024) 305.

[27] L. Pan, S. Sun, Y. Chen, P. Wang, J. Wang, X. Zhang, J.J. Zou, Z.L. Wang, Advances in piezo-phototronic effect enhanced photocatalysis and photoelectrocatalysis, Adv. Energy Mater. 10 (15) (2020) 2000214.

[28] X. Zhou, B. Shen, A. Lyubartsev, J. Zhai, N. Hedin, Semiconducting piezoelectric heterostructures for piezo- and piezophotocatalysis, Nano Energy 96 (2022) 107141.

[29] J. Zhang, Y. Sun, R. Feng, W. Liang, Z. Liang, W. Guo, I. Abdulhalim, J. Qu, C.-W. Qiu, L. Jiang, Plasmonic nanoparticle-film-assisted photoelectrochemical catalysis across the entire visible-NIR region, Nanoscale 11 (47) (2019) 23058–23064.

[30] Y. Wang, Y. Zhang, Z. Jiang, G. Jiang, Z. Zhao, Q. Wu, Y. Liu, Q. Xu, A. Duan, C. Xu, Controlled fabrication and enhanced visible-light photocatalytic hydrogen production of Au@CdS/MIL-101 heterostructure, Appl. Catal. B: Environ. 185 (2016) 307–314.

[31] R. Muthukumar, G. Balaji, S. Vadivel, The charge transfer pathway of g-C₃N₄ decorated Au/Ni₃(VO₄)₂ composites for highly efficient photocatalytic hydrogen evolution, Colloids Surf. A Physicochem. Eng. Asp. 655 (2022) 130183.

[32] W.-Q. Zhao, Q. Zhao, Z.-K. Song, L. Ma, X.-B. Chen, S.-J. Ding, L. Zhou, WO₃₋ₓ/PbS/Au ternary heterojunction nanostructures for visible-light-driven photocatalytic hydrogen generation, ACS Appl. Nano Mater. 5 (11) (2022) 16440–16450.

[33] T. Wei, J. Xu, C. Kan, L. Zhang, X. Zhu, Au tailored on g-C₃N₄/TiO₂ heterostructure for enhanced photocatalytic performance, J. Alloy. Compd. 894 (2022) 162338.

[34] D. Lu, J. Li, G. Lu, L. Qin, D. Liu, P. Sun, F. Liu, G. Lu, Enhanced photovoltaic properties of dye-sensitized solar cells using three-component CNF/TiO₂/Au heterostructure, J. Colloid Interface Sci. 542 (2019) 168–176.

[35] H. Zhou, X.-D. Zhu, P. Ge, T. Hang, S. Li, F. Guo, Y. Wu, C. Li, Synergistic coupling of surface plasmon resonance with metal-organic frameworks based biomimetic Z-

scheme catalyst for enhanced photoelectrochemical water splitting, Appl. Surf. Sci. 605 (2022) 154693.

[36] Z. Wang, Z. Zheng, Y. Xue, F. He, Y. Li, Acidic water oxidation on quantum dots of IrOₓ/graphdiyne, Adv. Energy Mater. 11 (32) (2021) 2101138.

[37] Z. Jia, Y. Li, Z. Zuo, H. Liu, C. Huang, Y. Li, Synthesis and properties of 2D carbon-graphdiyne, Acc. Chem. Res. 50 (10) (2017) 2470–2478.

[38] Y. Fang, Y. Liu, L. Qi, Y. Xue, Y. Li, 2D graphdiyne: an emerging carbon material, Chem. Soc. Rev. 51 (7) (2022) 2681–2709.

[39] X. Zheng, S. Chen, J. Li, H. Wu, C. Zhang, D. Zhang, X. Chen, Y. Gao, F. He, L. Hui, H. Liu, T. Jiu, N. Wang, G. Li, J. Xu, Y. Xue, C. Huang, C. Chen, Y. Guo, T.-B. Lu, D. Wang, L. Mao, J. Zhang, Y. Zhang, L. Chi, W. Guo, X.-H. Bu, H. Zhang, L. Dai, Y. Zhao, Y. Li, Two-dimensional carbon graphdiyne: Advances in fundamental and application research, ACS Nano 17 (15) (2023) 14309–14346.

[40] X. Bi, Q. Bai, L. Wang, F. Du, M. Liu, W.W. Yu, S. Li, J. Li, Z. Zhu, N. Sui, J. Zhang, Boron doped graphdiyne: A metal-free peroxidase mimetic nanozyme for antibacterial application, Nano Res 15 (2) (2021) 1446–1454.

[41] Q. Bai, K. Xiong, C. Zhang, L. Wang, W. Han, Q. Zhu, F. Du, W.W. Yu, N. Sui, Boosting charge separation in graphdiyne quantum dots/hollow tubular carbon nitride heterojunction for water pollutant degradation, J. Colloid Interface Sci. 646 (2023) 802–814.

[42] W. Ma, Y. Xue, S. Guo, Y. Jiang, F. Wu, P. Yu, L. Mao, Graphdiyne oxide: a new carbon nanozyme, Chem. Commun. 56 (38) (2020) 5115–5118.

[43] J. Liu, L. Wang, X. Shen, X. Gao, Y. Chen, H. Liu, Y. Liu, D. Yin, Y. Liu, W. Xu, R. Cai, M. You, M. Guo, Y. Wang, J. Li, Y. Li, C. Chen, Graphdiyne-templated palladium-nanoparticle assembly as a robust oxygen generator to attenuate tumor hypoxia, Nano Today 34 (2020) 100907.

[44] J. Li, X. Gao, Z. Li, J.H. Wang, L. Zhu, C. Yin, Y. Wang, X.B. Li, Z. Liu, J. Zhang, C. H. Tung, L.Z. Wu, Superhydrophilic graphdiyne accelerates interfacial mass/electron transportation to boost electrocatalytic and photoelectrocatalytic water oxidation activity, Adv. Funct. Mater. 29 (16) (2019) 1808079.

[45] X. Liao, X. Zhao, Z. Tan, C. Wang, W. Liu, Au nanoparticles in 2D bimetallic metal-organic frameworks with enhanced plasmonic nanozyme activity for antibacterial therapy, ACS Appl. Nano Mater. 5 (11) (2022) 16145–16153.

[46] H. Lv, Y. Liu, P. Zhao, Y. Bai, W. Cui, S. Shen, Y. Liu, Z. Wang, D.-G. Yu, Insight into the superior piezophotocatalytic performance of BaTiO₃//ZnO Janus nanofibrous heterostructures in the treatment of multi-pollutants from water, Appl. Catal. B: Environ. 330 (2023) 122623.

[47] J. Wu, W. Wang, Y. Tian, C. Song, H. Qiu, H. Xue, Piezotronic effect boosted photocatalytic performance of heterostructured BaTiO₃/TiO₂ nanofibers for degradation of organic pollutants, Nano Energy 77 (2020) 105122.

[48] Y. Zhao, S. Wang, Y. Ding, Z. Zhang, T. Huang, Y. Zhang, X. Wan, Z.L. Wang, L. Li, Piezotronic effect-augmented Cu₂₋ₓO-BaTiO₃ sonosensitizers for multifunctional cancer dynamic therapy, ACS Nano 16 (6) (2022) 9304–9316.

[49] W. Liu, P. Wang, Y. Ao, J. Chen, X. Gao, B. Jia, T. Ma, Directing charge transfer in a chemical-bonded BaTiO₃@ReS₂ schottky heterojunction for piezoelectric enhanced photocatalysis, Adv. Mater. 34 (29) (2022) 2202508.

[50] H. You, S. Li, Y. Fan, X. Guo, Z. Lin, R. Ding, X. Cheng, H. Zhang, T.W.B. Lo, J. Hao, Y. Zhu, H.-Y. Tam, D. Lei, C.-H. Lam, H. Huang, Accelerated pyro-catalytic hydrogen production enabled by plasmonic local heating of Au on pyroelectric BaTiO₃ nanoparticles, Nat. Commun. 13 (1) (2022) 6144.

[51] C. Zhang, Y. Xue, X. Zheng, L. Qi, Y. Li, Loaded Cu-Er metal iso-atoms on graphdiyne for artificial photosynthesis, Mater. Today 66 (2023) 72–83.

[52] Q. Bai, J. Zhang, Y. Yu, C. Zhang, Y. Jiang, D. Yang, M. Liu, L. Wang, F. Du, N. Sui, Z. Zhu, Piezoelectric activatable nanozyme-based skin patch for rapid wound disinfection, ACS Appl. Mater. Interfaces 14 (23) (2022) 26455–26468.

[53] C. Lu, Y. Yang, J. Wang, R. Fu, X. Zhao, L. Zhao, Y. Ming, Y. Hu, H. Lin, X. Tao, Y. Li, W. Chen, High-performance graphdiyne-based electrochemical actuators, Nat. Commun. 9 (1) (2018) 752.

[54] X. Chen, X. Zheng, L. Qi, Y. Xue, Y. Li, Conversion of interfacial chemical bonds for inducing efficient photoelectrocatalytic water splitting, ACS Mater. Au 2 (3) (2022) 321–329.

[55] J. Yan, Y. Han, S. Xia, X. Wang, Y. Zhang, J. Yu, B. Ding, Polymer template synthesis of flexible BaTiO₃ crystal nanofibers, Adv. Funct. Mater. 29 (51) (2019) 1907919.

[56] C. Ma, S. Feng, J. Zhou, R. Chen, Y. Wei, H. Liu, S. Wang, Enhancement of H₂O₂ decomposition efficiency by the co-catalytic effect of iron phosphide on the Fenton reaction for the degradation of methylene blue, Appl. Catal. B: Environ. 259 (2019) 118015.

[57] S. Shi, Y. Jiang, Y. Yu, M. Liang, Q. Bai, L. Wang, D. Yang, N. Sui, Z. Zhu, Piezo-augmented and photocatalytic nanozyme integrated microneedles for antibacterial and anti-inflammatory combination therapy, Adv. Funct. Mater. 33 (10) (2022) 2210850.

[58] X. Yu, S. Wang, X. Zhang, A. Qi, X. Qiao, Z. Liu, M. Wu, L. Li, Z.L. Wang, Heterostructured nanorod array with piezophototronic and plasmonic effect for photodynamic bacteria killing and wound healing, Nano Energy 46 (2018) 29–38.

[59] Y. Kong, X. Li, L. Wang, Z. Zhang, X. Feng, J. Liu, C. Chen, L. Tong, J. Zhang, Rapid synthesis of graphdiyne films on hydrogel at the supspreading interface for antibacteria, ACS Nano 16 (7) (2022) 11338–11345.

[60] H. Zheng, X. Li, K. Zhu, P. Liang, M. Wu, Y. Rao, R. Jian, F. Shi, J. Wang, K. Yan, J. Liu, Semiconducting BaTiO₃@C core-shell structure for improving piezo-photocatalytic performance, Nano Energy 93 (2022) 106831.

[61] X. Zhou, S. Wu, C. Li, F. Yan, H. Bai, B. Shen, H. Zeng, J. Zhai, Piezophototronic effect in enhancing charge carrier separation and transfer in ZnO/BaTiO₃ heterostructures for high-efficiency catalytic oxidation, Nano Energy 66 (2019) 104127.

[62] X. Liao, Q. Xu, H. Sun, W. Liu, Y. Chen, X.-H. Xia, C. Wang, Plasmonic nanozymes: localized surface plasmonic resonance regulates reaction kinetics and antibacterial performance, J. Phys. Chem. Lett. 13 (1) (2022) 312–323.

[63] H. Yang, L.Q. He, Y.W. Hu, X. Lu, G.R. Li, B. Liu, B. Ren, Y. Tong, P.P. Fang, Quantitative detection of photothermal and photoelectrocatalytic effects induced by SPR from Au@Pt nanoparticles, Angew. Chem. Int. Ed. 54 (39) (2015) 11462–11466.

[64] D.Y. Wei, M.F. Yue, S.N. Qin, S. Zhang, Y.F. Wu, G.Y. Xu, H. Zhang, Z.Q. Tian, J. F. Li, In situ Raman observation of oxygen activation and reaction at platinum-ceria interfaces during CO oxidation, J. Am. Chem. Soc. 143 (38) (2021) 15635–15643.

[65] H.-Q. Chen, L. Zou, D.-Y. Wei, L.-L. Zheng, Y.-F. Wu, H. Zhang, J.-F. Li, In situ studies of energy-related electrochemical reactions using Raman and X-ray absorption spectroscopy, Chin. J. Catal. 43 (1) (2022) 33–46.

[66] X. Zhao, Z. Li, J. Yu, C. Li, S. Xu, F. Li, C. Zhang, B. Man, C. Zhang, Plasmonic and bi-piezoelectric enhanced photocatalysis using PVDF/ZnO/Au nanobrush, Nanophotonics 11 (14) (2022) 3339–3349.

[67] L. Wolski, M. Ziolek, Insight into pathways of methylene blue degradation with H_2O_2 over mono and bimetallic Nb, Zn oxides, Appl. Catal. B: Environ. 224 (2018) 634–647.